AGU ADVANCING EARTH AND SPACE SCIENCE

Earth and Space Science

RESEARCH ARTICLE
10.1029/2022EA002763

Key Points:

- A retrieval algorithm based on daytime Rayleigh scattered radiation near 350 nm is proposed
- The algorithm retrieves temperature profile from Ozone Mapping and Profiler Suite Limb Profiler in the 35–70 km altitude range
- We compare the new temperature profiles to other measurements over the same region

Correspondence to:
Z. Chen,
zhong.chen@ssaihq.com

Citation:
Chen, Z., Schwartz, M. J., Bhartia, P. K., Schoeberl, M., Kramarova, N., Jaross, G., & DeLand, M. (2023). Mesospheric and upper stratospheric temperatures from OMPS-LP. *Earth and Space Science*, *10*, e2022EA002763. https://doi.org/10.1029/2022EA002763

Received 28 NOV 2022
Accepted 12 APR 2023

Author Contributions:
Conceptualization: Pawan K. Bhartia
Investigation: Zhong Chen
Methodology: Pawan K. Bhartia
Project Administration: Mark Schoeberl
Validation: Michael J. Schwartz
Writing – original draft: Zhong Chen
Writing – review & editing: Mark Schoeberl, Natalya Kramarova, Glen Jaross, Matthew DeLand

Mesospheric and Upper Stratospheric Temperatures From OMPS-LP

Zhong Chen[1,2], Michael J. Schwartz[3], Pawan K. Bhartia[2], Mark Schoeberl[4], Natalya Kramarova[2], Glen Jaross[2], and Matthew DeLand[1]

[1]Science Systems and Applications, Inc., Lanham, MD, USA, [2]NASA Goddard Space Flight Center, Greenbelt, MD, USA, [3]Jet Propulsion Laboratory, California Institute of Technology, Pasadena, CA, USA, [4]Science and Technology Corporation, Hampton, VA, USA

Abstract We report the development of a temperature profile data set from the Ozone Mapping and Profiler Suite Limb Profiler (OMPS-LP) instrument on the Suomi NPP satellite. The data set covers a roughly 10 year period from 2012 to 2022, and temperatures are provided in the altitude range between 35 and 70 km. The algorithm uses daytime Rayleigh scattered radiation near 350 nm to estimate atmospheric density profiles, which are vertically integrated using the hydrostatic equation to estimate atmospheric pressure. Temperature profiles are then derived using the ideal gas law. Spectral structures in the OMPS-LP radiances are a source of systematic errors that limit the absolute accuracy to ±2 K. However, since the systematic errors do not change significantly over time, the relative accuracy is better than ±1 K. Our temperature data set has been designed to supplement global temperature maps produced by assimilation of data from traditional meteorological sensors, including GNSS radio occultation sensors, that provide high quality atmospheric temperature profiles up to 40–55 km. We show comparisons to other co-located temperature datasets to validate our product.

1. Introduction

Changes in upper stratosphere and lower mesosphere temperatures are early indicators of overall climate-driven processes. For example, increasing CO_2 is expected to produce cooling in these regions (Roble & Dickinson, 1989), and such cooling has already been observed by a number of instruments. Recently, Zhao et al. (2020) detected a cooling trend of ~0 to −0.14 K/decade at all latitudes using the annual mean temperatures from Sounding of the Atmosphere Using Broadband Emission Radiometry (SABER) instrument from 2002 to 2019. Li et al. (2020) used merged Halogen Occultation Experiment (HALOE) and SABER observations between 1991 and 2018 to investigate cooling trends between 40 and 80 km altitude with a maximum value of ~1.2 K/decade. In the summer polar mesosphere, Bailey et al. (2021) identified a cooling trend of 1–2 K/decade using Solar Occultation for Ice Experiment (SOFIE) measurements. Such cooling trends will likely increase the abundance of Polar Mesospheric Clouds (PMCs). All of these satellite-based temperature trends are inferred from data produced by systems that have functioned well past their expected lifetimes and/or require merging of data sets generated using different techniques. With the Suomi National Polar-orbiting Partnership/Joint Polar Satellite System (SNPP/JPSS) systems, which are expected to operate into the 2030s, we have the opportunity to generate a temperature record from a series of Ozone Mapping and Profiler Suite (OMPS) Limb Profiler (LP) (OMPS-LP) instruments that spans decades. This paper describes our technique for producing temperature profiles between 35 and 70 km from Rayleigh scattered radiance fields.

Upper atmospheric temperatures have been measured using a variety of techniques including in situ measurements from occasional very high altitude balloons, GNSS radio occultation, satellite microwave, IR measurements, and ground based lidar. One of the first satellite global temperature and density measurements in the 40–92 km altitude range was derived from the Solar Mesosphere Explorer (SME) limb radiance profiles at 304, 313, and 442 nm (Clancy et al., 1994). Shepherd et al. (2001) retrieved temperature from 65 to 90 km using radiance data at 553 nm from the Wind Imaging Interferometer (WINDII) instrument. Sheese et al. (2012) retrieved temperature profiles using Optical Spectrograph and InfraRed Imaging System (OSIRIS) bright limb observations at 318.5 and 347.5 nm in the altitude range 45–85 km, and Hauchecorne et al. (2019) created temperature and density profiles from 35 to 85 km using limb radiances in the spectral band 420–480 nm from the Global Ozone Monitoring by Occultation of Stars (GOMOS) instrument on ENVISAT. Among the currently operating instruments, Microwave Limb Sounder (MLS) and SABER temperatures are the primary source of stratospheric and mesospheric temperature used in assimilation systems (Gelaro et al., 2017; Schwartz et al., 2008). MLS is scheduled to be decommissioned by 2024, and SABER is beyond its estimated operating lifetime, which means that the community could lose its primary sources of temperature measurements in the upper stratosphere and lower troposphere.

In this paper, we show how upper stratospheric temperatures can also be produced from the OMPS-LP instrument onboard the Suomi National Polar-orbiting Partnership (SNPP) satellite (Flynn et al., 2007). OMPS-LP was launched in October 2011, into a sun synchronous orbit with 13:30 local ascending equator crossing time. The primary data contributions of OMPS-LP to the SNPP mission are measurements of ozone, aerosol extinction and cloud height (Chen, 2022; Chen et al., 2016, 2018, 2020; Kramarova et al., 2018; Loughman et al., 2018; Rault & Loughman, 2013). OMPS-LP on SNPP will be followed by three additional instruments on JPSS-2, 3, and 4, the last scheduled to launch in 2032. OMPS-LP can therefore provide upper stratospheric temperature information for assimilation systems for the next decade and beyond.

Below we describe our temperature algorithm and present error analysis using a combination of analytical and simulation methods to establish a baseline accuracy for retrieved temperature profiles. To assess the quality and capabilities of this new data product, we compare the new temperature profiles to other measurements over the same region.

2. The OMPS-LP Sensor

The OMPS-LP sensor measures solar photons scattered from the atmosphere in the ultraviolet (UV) and visible (VIS) spectral ranges (Jaross et al., 2014). The UV measurements between 290 and 400 nm are used to retrieve ozone concentration in the upper and middle stratosphere, and visible measurements between 500 and 700 nm are used to retrieve ozone in the lower stratosphere (McPeters et al., 2000). Aerosol extinction retrievals are produced at various wavelengths between 500 and 1,000 nm (Taha et al., 2021). To expand its spatial coverage, the LP sensor simultaneously images three vertical profiles of the atmosphere separated in longitude by approximately 250 km. With 14.5 orbits per day and with each slit providing approximately 1° latitude sampling, the LP sensor provides full global coverage every 3–4 days (Kramarova et al., 2018). In future JPSS missions the orbital ground tracks will be offset from each other, thereby improving the daily global coverage of the combined products.

Each LP slit has a 1.85° field of view (FOV) that corresponds to a 105 km vertical extent at the tangent point. Seasonal and orbital variations in pointing place some of this view at the Earth's surface, but the maximum altitude always extends to at least 80 km. The charge coupled device (CCD) detector used by LP simultaneously collects scattered solar radiances from all altitudes in the spectral range between 290 and 1,000 nm. Use of a prism for spectral dispersion results in a spectral resolution that varies from 1 nm at the short end of the spectrum to about 40 nm at the long end. The vertical sampling is limited by the detector pixel size, which is 1 km when projected to the tangent point. The instantaneous pixel FOV is approximately 1.2 km, which degrades through motion and atmospheric effects to 1.3–1.7 km.

To maintain adequate signal levels over its full altitude range each slit produces multiple images of the vertical profile. Low altitude (bright) signals are measured with a small aperture and high altitude (low intensity) signals are measured with a large aperture. Both are measured with interleaved short and long integration times. All 12 sets of spectra (three slits, two apertures, and two integration times) are captured on a single focal plane and a portion of each is sent to the ground for merging into a combined radiance product for each slit. Data bandwidth limitations mean that some wavelengths and altitudes are not downloaded and are therefore unavailable for retrieval processes. Because the images at the detector are distorted, the raw pixel data are passed through a 2-D interpolation step on the ground to yield sets of monochromatic radiances on uniform vertical scales. All OMPS-LP retrieved products to date are based on these gridded radiances.

3. Algorithm Description

3.1. Radiative Transfer Model

We use measured radiances near 350 nm to estimate temperature profiles from OMPS-LP because our temperature retrieval relies on the non-absorbing spectral region around 350 nm, where Rayleigh scattering is the prime mechanism to redirect light to the LS sensor. We use a radiative transfer model (RTM) to calculate the

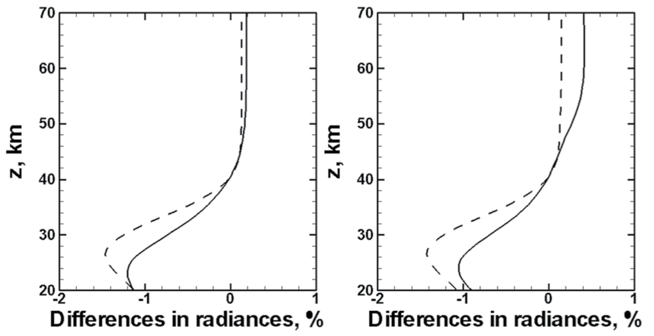

Figure 1. An example showing % differences in the calculated radiances at 350 nm with and without O_3 (solid line) and with and without NO_2 (dashed line) normalized at 40.5 km for single scattered radiances I_{ss} (left) and total radiance (including multiply scattered) I_{tot} (right).

limb-scattered radiances (LSRs) as a function of altitude. This calculation requires vertical profiles of neutral gas density, aerosols density, and of any trace gases that absorb at 350 nm. At 350 nm, O_3 and NO_2 absorb only significantly below 40 km (Figure 1). We use the Gauss–Seidel limb scattering RTM (Loughman et al., 2015) to calculate the LSR. The RTM accounts for both single-scattering along the line-of-sight (LOS) and multiple-scattering from outside the LOS. The RTM assumes that the atmosphere is horizontally homogeneous along the LOS. We use a 1-D RTM, which assumes that the atmosphere is horizontally homogeneous along the LOS. We note that in the limb geometry, neutral density profiles extending up to 95 km are needed to accurately calculate the LSR at 75 km.

Below 40 km, the scattering effect of aerosols can also become important at 350 nm. To account for aerosol scattering, we use extinction profiles retrieved from LP radiances at 675 nm (Chen et al., 2018, 2020; Loughman et al., 2018). Aerosol scattering contributions to 350 nm radiances are then calculated assuming Mie scattering, using the same particle size distribution and refractive indices assumed in retrieving 675 nm aerosols (Chen et al., 2020). Note that the employed algorithm differs from that of Taha et al. (2021) in that radiances are normalized at 40.5 km, rather than at 37.5 km, reducing the effects of scattered light at the long-wavelength end of the band. In some years, the quasi-biennial oscillation (QBO) can loft considerable amounts of aerosols above 35 km in the tropical latitudes, leading to significant underestimation of aerosol at 35 km when a lower normalization altitude is used. Figure 2 shows an example of the retrieved aerosol extinctions at 675 nm and their effect upon 350 nm radiances calculated using the RTM. Though the aerosol amounts at this time are near the maximum seen in the LP record, their effect on 350 nm radiances is relatively modest. Hence, we use the Chen et al. (2020) data set for our aerosol scattering calculations. We recommend using this data set for users interested in aerosol effects above 30 km. It can be obtained from the lead author by special request.

3.2. Pressure Calculation

We wish to retrieve temperature profiles but the RTM requires a density profile, so we first calculate a pressure profile by hydrostatic integration. Density is calculated using the gas law. Our starting temperature profile T(z) is obtained from a data set of temperature profiles produced by assimilating meteorological data. We use the NASA Global Modeling Assimilation Office (GMAO) Forward Processing for Instrument Teams (FP-IT) data product (Gelaro et al., 2017), which does not assimilate MLS temperature data. These profiles are provided at every 1 km

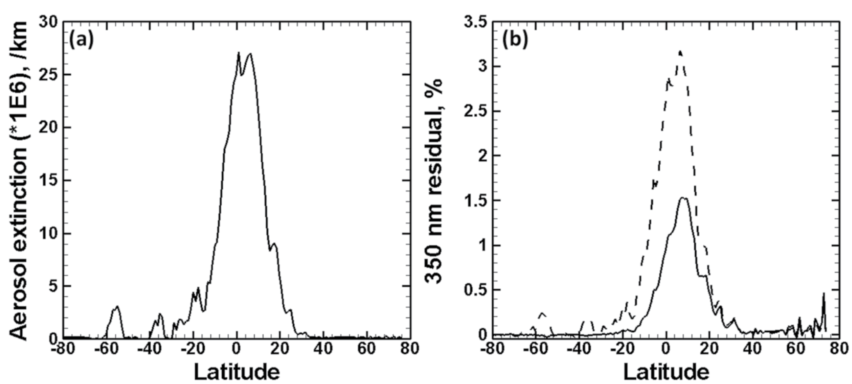

Figure 2. Effect of aerosols on 350 nm radiances. (a) Latitude dependence of 675 nm aerosol extinction at 35.5 km for a 21 February 2017 orbit. (b) % change in calculated 350 nm radiances at 35.5 km due to aerosols for singly scattered radiances I_{ss} (solid line) and the total radiance (including multiply scattered) I_{tot} (dashed line) normalized at 40.5 km. The observed asymmetry between the NH and SH is caused by asymmetry in the aerosol phase function as a function of scattering angle, and the fact that Ozone Mapping and Profiler Suite Limb Profiler (OMPS LP) observations occur with backward scattering geometry ($\theta > 90°$) in the Southern Hemisphere and forward scattering geometry ($\theta < 90°$) in the Northern Hemisphere. Loughman et al. (2018) describes the importance of viewing geometry for OMPS LP measurements in more detail.

from the surface to 80 km. We extend them to 100 km by making an isothermal assumption at higher altitudes, that is, we assume T (80) from 80 to 100 km. The pressure profile $P_o(z)$ is calculated as follows.

$$\ln P_o(z) = \ln P_o(z) - c \int_{z=z_0}^{z} \frac{g(l, z)}{T(z)} dz \quad (1)$$

where g is the gravity in m/s^2 and c is the constant of value 0.003484 in K·s^2/m^2, z is the altitude in m and l is the latitude.

We start the integration at $z_o = 30.5$ km using the trapezoidal rule. Below 30 km, 350 nm LSR are significantly affected by aerosols, and accurate aerosol corrections at this wavelength are quite difficult. Since GMAO_FP temperature and pressure data are considered quite reliable below ∼35 km, retrievals below 30 km from OMPS-LP provide little additional benefit. The retrieval is nearly independent of the starting temperature profile, but we will explore this dependence in Sections 4, 6, and 7.1.

3.3. Retrieval of Atmospheric Density Profile

To retrieve vertical profiles of air density from measured LSR we apply the Chahine Relaxation Method (Chahine, 1970). This algorithm is well suited for limb retrievals, since it works best when the weighting functions are narrow, and is given by the following simple formula.

$$\boldsymbol{x}_{n+1}^{i} = \boldsymbol{x}_{n}^{i} \frac{\boldsymbol{y}_{mc}^{j}}{\boldsymbol{y}_{n}^{j}}, \quad \mathrm{n} = 1, 2 \ldots \quad (2)$$

where $\boldsymbol{x}_n^i$ represents the air density at the altitude z_i retrieved after n iterations, $\boldsymbol{y}_\mathrm{mc}^j$ is the single scattering (SS) component of the measured radiances at tangent height $th_j = z_i$, the subscript 'mc' means the measured radiance corrected for several errors that we discuss in Section 5, and $\boldsymbol{y}_n^j$ is the SS radiances calculated from the profile $\boldsymbol{x}_n$ with components $\boldsymbol{x}_n^i$. We use extrapolated GMAO FP temperatures, described above, as $\boldsymbol{x}_1^i$. We find that the iteration converges well after five iterations ($n = 5$).

3.4. Multiple Scattering Correction

As mentioned in Section 3.3, we use the SS component of the measured radiance in our retrieval algorithm. In this section we describe the procedure of making this estimation.

At 350 nm a major fraction of the measured radiance is scattered from the atmosphere along the LOS. The remainder is multiply scattered (MS) radiation, first scattered from outside to the LOS, and then scattered by the atmosphere along the LOS to reach the instrument. Most of this MS radiation comes from a cone extending below the instrument whose apex is at the tangent height, and the base extends to the horizon. Since this cone can contain a mixture of cloudy and clear sky, aerosols, and clouds of different types and shapes, there is no exact method of calculating this radiation. We use a technique to estimate this MS contribution that was developed by Mateer et al. (1971) for the modeling of similar radiation viewed by a nadir-viewing satellite instrument. In their method, MS radiation is modeled as if it comes from an aerosol/cloud-free atmosphere bounded by a Lambertian reflecting surface located at the Earth's surface. Reflectance is calculated from the measured radiances at the top the atmosphere and is referred to as Lambert-equivalent reflectivity (LER) of the scene. We use a similar method for the limb geometry, except that LER is calculated from LSR at 40.5 km. Since there are typically no aerosols at this altitude, the calculation requires only the atmospheric (including any trace gases) density profiles.

Figures 3a–3c show the ratio of SS and total (SS + MS) radiances at 350 nm for different solar zenith angles, calculated assuming a Lambertian reflecting surface of reflectivity $R = 0$ and 1. We note that the effect of non-zero reflectivity is largely to shift the ratio curve by a constant multiplicative factor. This result allows us to greatly reduce the effect of R by normalizing the radiances at 40.5 km. The normalized ratio curves are shown in Figures 3d–3f. A key assumption in our algorithm is that the normalization also makes the algorithm insensitive to the assumptions made in using the LER concept. Note that altitude normalization also reduces instrument calibration errors. Though RTMs are not available to verify this assumption for real clouds with complex vertical and horizontal structures, we find that this normalization reduces the sensitivity of the MS calculation to a number of unmodeled error sources, including the effects of surface pressure and polarization. This allows us to assume

10.1029/2022EA002763

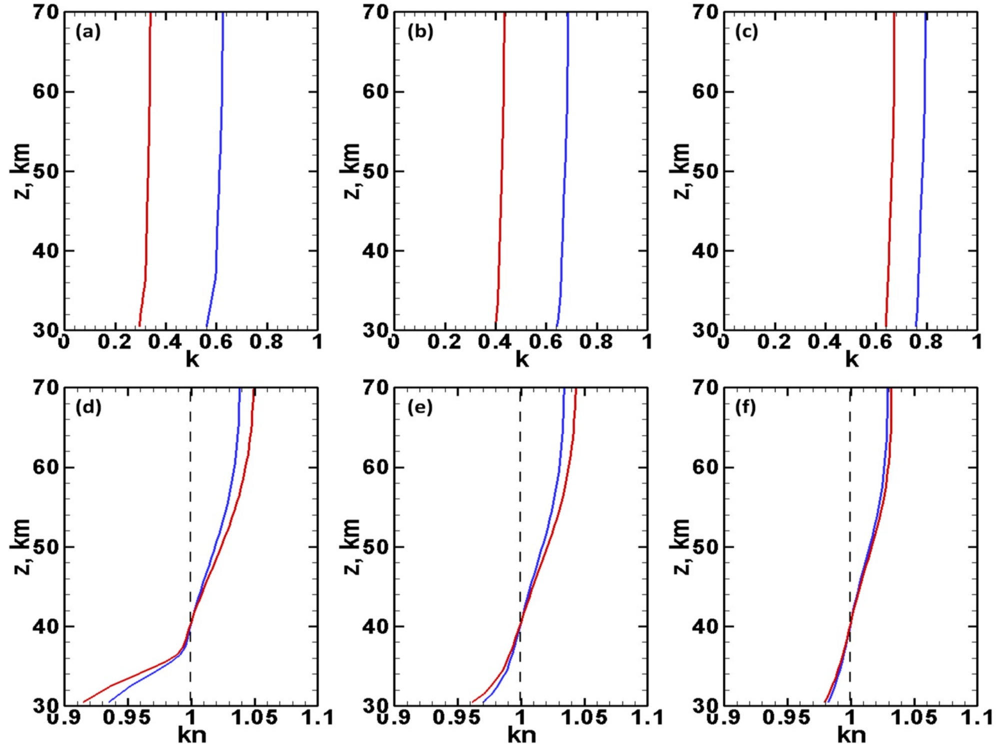

Figure 3. The upper panels (a–c) show k, the ratio of singly scattered and total scattered (single plus multiple scattered) radiance at 350 nm for two surface reflectivities, $R = 0$ (blue) and $R = 1$ (red), at three solar zenith angles SZAs (19° (a), 39° (b), and 69° (c)). Even at $R = 0$, only about 60% of the radiation is singly scattered at the smallest solar zenith angle, reducing to 30% at $R = 1$. The lower panels (d–f) show $k_{n,}$ k normalized at 40.5 km. Altitude normalization greatly reduces R dependence.

that the surface is located at 1,000 hPa, even for high terrain and high clouds, and allows us to use a much faster scalar RTM.

Since the last scattering of the MS radiation occurs along the LOS, as does the SS radiation, in absence of aerosols, the ratio $k = I_{ss}/I_{tot}$, where I_{ss}, is the SS radiation and I_{tot} is the total radiation, is fairly insensitive to the atmospheric density profile, including the profiles of trace gases. This is the case even at wavelengths where O_3 is a significant absorber.

Combining all these ideas to estimate the SS component of the measured radiances we multiply the altitude-normalized measured radiance by the factor k_n, calculated using first guess profiles of neutral and absorbing gases, where

$$k_n = [I_{ss}(z)/I_{ss}(z_n)]/[I_{tot}(z)/I_{tot}(z_n)] \quad (3)$$

where z is the altitude, and z_n is the normalization altitude (40.5 km).

3.5. Estimation of Temperature Profile

Given the retrieved atmospheric density, we estimate the final pressure profile by integrating the hydrostatic equation, and then use the gas law to estimate the temperature profile. To reduce quadrature errors this integration starts at a high altitude and goes down. The method is similar to that used by Rayleigh lidar systems (Hauchecorne and Chanin, 1980; Whiteway & Carswell, 1995). The quadrature is done as follows.

$$P(z) = P(z_0) + \int_{z=z_0}^{z} g(l,z)\rho(z)dz \quad (4)$$

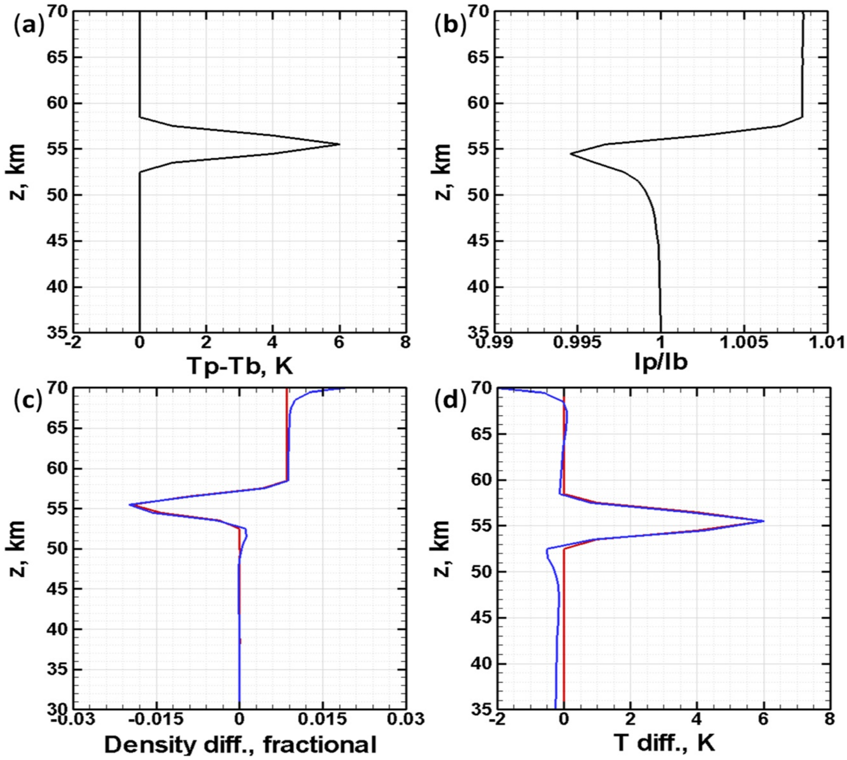

Figure 4. (a) Difference between perturbed temperature (T_p) and baseline temperature (T_b). (b) Ratio of perturbed radiance (I_p) to baseline radiance (I_b) at 350 nm. (c) Differences between perturbed density (ρ_p) and baseline density (ρ_b) (ρ_p/ρ_b −1, red), and between retrieved density (ρ_r) and baseline density (ρ_r) (ρ_r/ρ_b −1, blue) after five iterations. (d) Differences between T_p and T_b (T_p–T_b, red), and retrieved temperature T_r and T_b (T_r–T_b, blue). The kinks at 70 km in retrieved air density and temperature are caused by the fact that we terminate the retrieval at that altitude in this simulation. See text for more explanation.

3.6. Integrating Equation 4 Using a Modified Trapezoidal Rule

$$P(z) = P(z_0) + \sum_{z=z_0-\Delta z}^{z} g\left(\lambda, z - \frac{\Delta z}{2}\right)\rho\left(z - \frac{\Delta z}{2}\right)\Delta z \tag{5}$$

$$\rho\left(z - \frac{\Delta z}{2}\right) = \sqrt{\rho(z)\rho(z-\Delta z)} \tag{6}$$

$$T(z) = \frac{P(z)}{R\rho(z)} \tag{7}$$

where $\rho(z)$ is the mass density profile. Since the atmospheric density varies exponentially with height we use the geometric mean rather than arithmetic mean in the trapezoidal rule. Calculations show that this method works well.

4. Perturbation Analysis

In this section we examine the algorithm sensitivity to 3 km wide perturbations in a baseline temperature profile using synthetic data. We simulate synthetic measured radiances with a SS code using climatological temperature profile and assume that there are no instrumental errors. We have three objectives in doing this sensitivity study: (a) to estimate the sensitivity of LSR to temperature perturbations, (b) to test the convergence property of the retrieval algorithm, and (c) to evaluate the vertical resolution of the retrieved temperature profile. Figure 4a shows the applied temperature perturbation, and Figure 4b shows the effect of this perturbation on the simulated measurements. Note that ±6 K (~3%) perturbation produces only 0.5% reduction in the simulated radiances, and that the effect of perturbation is not local; it extends all the way to infinity increasing radiances above perturbed layers by ~0.8%. This occurs because we are measuring the density and deriving the temperature so changes in density are coupled to higher levels through the hydrostatic equation. The very low sensitivity of the LSR requires pre-processing of our measurements to reduce systematic and random errors. We discuss this approach in Section 5.

Figure 4c shows the input and retrieved density perturbation. It is important to note that the input density perturbations extend to infinity but in this simulation we are terminating our retrievals at 70.5 km, that is, we use baseline density profile above 70.5 km. This produces a kink in the retrieved density profile near 70 km. A similar kink appears in the estimated T profile (Figure 4d). Since we do not expect our retrieved temperature profiles to be accurate near the top altitude, we choose to ignore this error.

Our analysis shows that it is possible to retrieve a 3 km wide temperature perturbation from LSR. We have done a similar study, narrowing the perturbation to 2 km, with similar results. However, since the horizontal resolution of a limb measurement is coarse (~200 km), we consider 3 km as the nominal vertical resolution of our retrievals.

5. Pre-Processing of Measured Radiances

As discussed in Section 4, the sensitivity of LSR to temperature perturbation is quite weak (~0.07%/K), so careful minimization of systematic and random errors is required in production of a useful temperature product. In this section we discuss how we process the measured radiance near 350 nm to do this. We take advantage of the fact that the fractional change in LSR due to temperature perturbation is independent of wavelength. This allows us to look at OMPS-LP measurements near 350 nm to minimize errors that vary with wavelength.

5.1. Screening of Data Affected by Charged Particles

The South Atlantic charged particle anomaly (SAA) is a significant cause of bad data in OMPS-LP measurements (Jaross et al., 2014). Since it affects the CCD pixels randomly, we detect such effects by looking at the standard deviation of the logarithm of radiances at 11 wavelengths centered at 350 nm. Figures 5 and 6 show large increases in the standard deviation in the Southern Hemisphere compared to the baseline value. The latitude range where these effects occur in LP data is shifted relative to the SAA location because the tangent point is approximately 27° south from the spacecraft position, where the CCD is located. However, one also sees increases at other latitudes, presumably also resulting from charged particle interactions with the CCD.

5.2. Correction of Vertical Structures

OMPS-LP radiances used in our retrievals have known systematic errors that produce non-geophysical vertical structures in the ratio of radiances and irradiances. At 350 nm these structures have peak-to-peak value of ~1%. It is not known what causes these structures, but since they produce fixed patterns on the CCD, the altitude of these structures in the limb view varies with latitude as the spacecraft maintains geodetic pointing for its nadir-viewing instruments. Since these structures vary pseudo-randomly with wavelength they are reduced by spectral averaging. We compare the average of the log radiances over 11 wavelengths in the range from 345 to 355 nm centered at 350 nm with 350 nm measurements to estimate this error (E), as described below.

$$E = \ln I_m(\lambda_{350}) - \sum_{i=1}^{11} \ln I_m(\lambda_i)/11 \tag{8}$$

where I_m is the measured radiance at wavelength λ. We use E to correct our measured radiances (Figure 7). Note that even if the vertical structures were perfectly random, 11 wavelength averaging will not remove them completely. With averaging the error is reduced from 1% peak-to-peak to about 0.3%. Given 0.07%/K sensitivity of LSR, this will amount to 4 K peak-to-peak error in temperature (roughly 1 K standard deviation). This is one of the primary sources of systematic errors in our measurements. The E correction also reduces the effect of random noise by a factor of three. This produces 1 sigma measurement precision of ~±0.07%, or ±1 K in temperature. The combined effect of systematic and random error is ~1.4 K (1 sigma) for each retrieval. The initial version of the retrieval algorithm uses a single wavelength at 350 nm because the quality of the stray light correction for OMPS LP wavelengths for other wavelengths was uncertain at that time. The average of all of these channels will be used in future work.

10.1029/2022EA002763

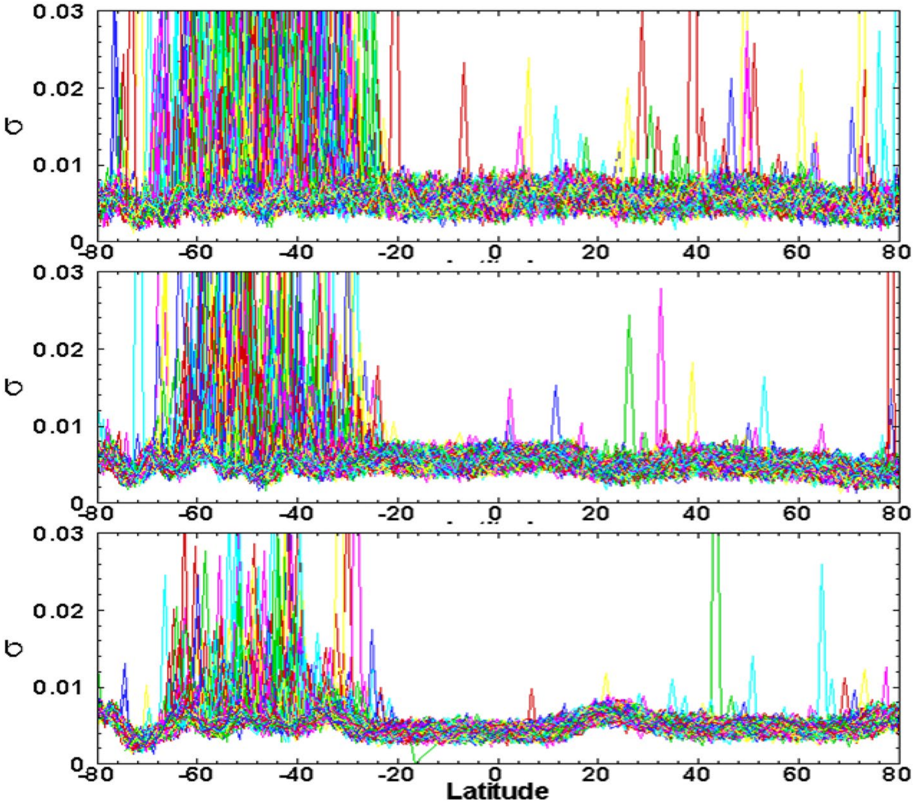

Figure 5. Standard deviation (σ) of log of measured radiances from 426 orbits in March 2017 at 65.5 km (top), 60.5 km (middle) and 55.5 km (bottom). The σ is calculated using 11 wavelengths between 340 and 355 nm centered at 350 nm. The baseline values represent measurement noise plus other instrumental uncertainties. Large σ values mostly occur in the SAA region but they can occur elsewhere as well. Note the apparent latitude of South Atlantic charged particle anomaly effects is shifted southward from their location above earth's surface because of Ozone Mapping and Profiler Suite Limb Profiler measurement geometry.

5.3. Screening of Data Affected by PMC

Polar mesospheric clouds (PMCs), which occur at 80–85 km at high latitudes during summer months, can cause enhanced signals at lower altitudes when they appear in the line of sight (DeLand & Gorkavyi, 2020). To identify data affected by PMCs, we examine the radiance residuals at 65.5 km, defined as log (I_{mc})-log (I_c), where I_{mc} is the single scattered component of the measured radiance at 350 nm, corrected for the effects described in Sections 5.1 and 5.2, and I_c is the radiance calculated using first guess profiles. Figures 8 and 9 show an example of data screened by this method.

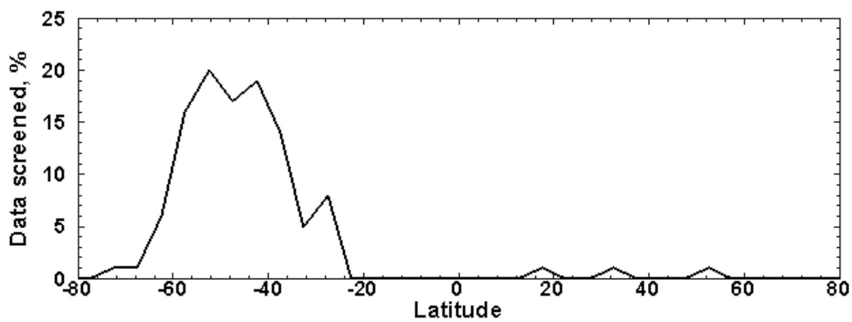

Figure 6. Percent of data screened on a typical day (23 March 2017) by putting a threshold at σ of 0.013 (see Figure 5). Measured radiance profiles are removed if the σ exceeds this threshold at any altitude between 35.5 and 75.5 km. This is because the current algorithm requires measured radiances at all these altitudes. Most of the screened data occur in the South Atlantic Anomaly region, but they can occur elsewhere.

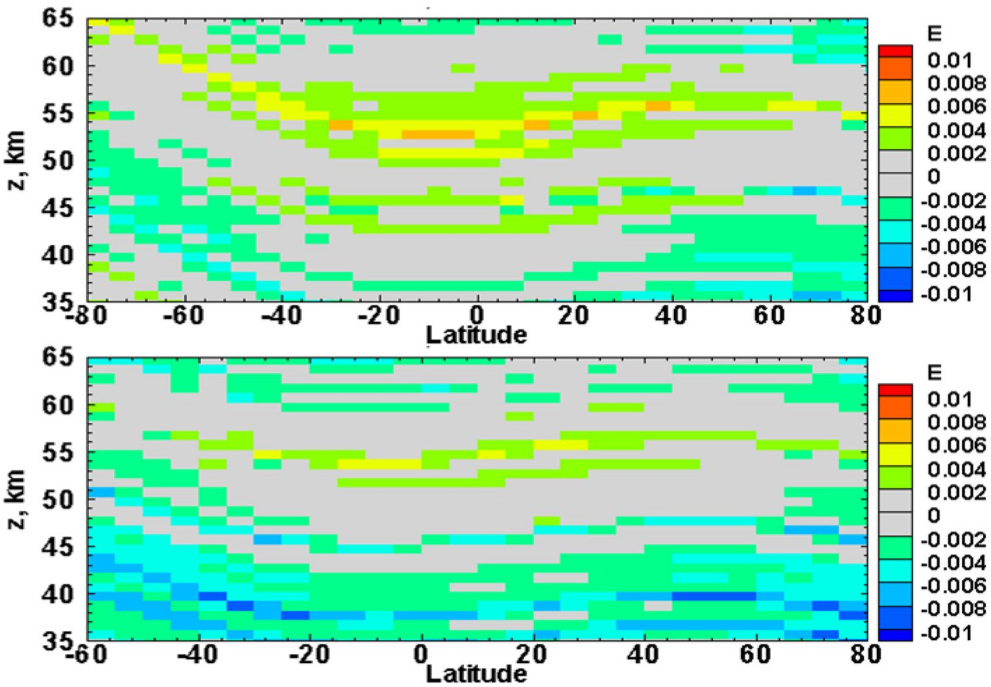

Figure 7. Systematic errors in Limb Profiler radiances at 350 nm (E) as a function of latitude and altitude estimated using the procedure described in the text. The upper panel shows data for March 23, the lower panel for 11 June 2017. The figure shows that the structures vary with season.

6. Internal Validation

In this section, we describe techniques for identifying bad data through internal consistency checks. Though these methods cannot detect all errors, they can be useful for isolating subtle errors that may be hard to detect by comparison with other instruments. They also highlight areas where such comparisons should be targeted. We

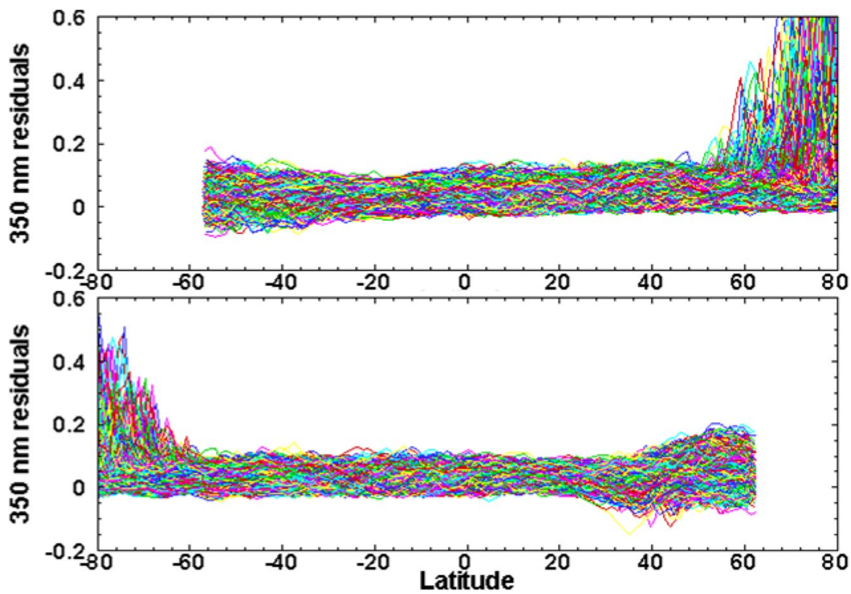

Figure 8. Shows 350 nm radiance residuals (measured minus calculated log of radiances) at 65.5 km as a function of latitude for 2 months of data, June 2017 (top) and December 2017 (bottom). Larger residuals at mid- and high-latitudes are caused by the presence of polar mesospheric clouds along the line-of-sight of the instrument.

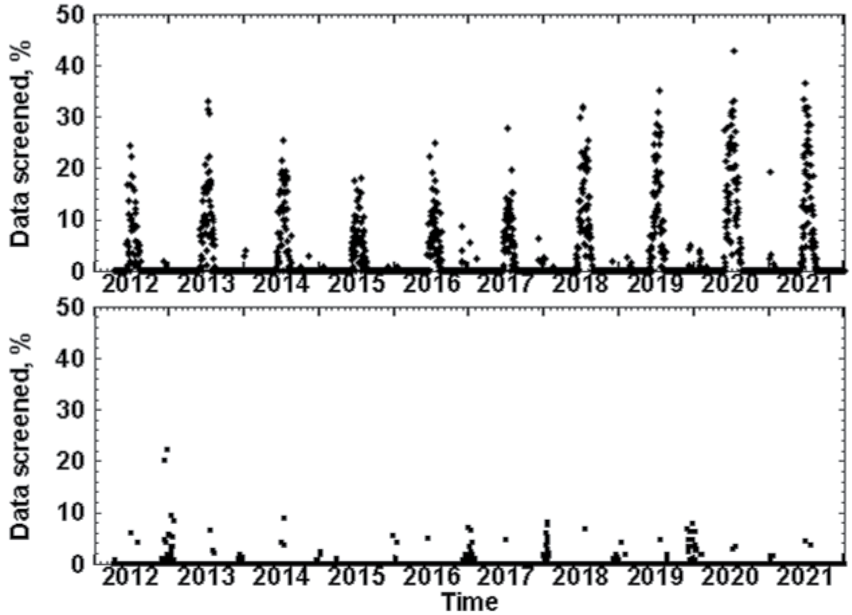

Figure 9. Fraction of data screened in 55°N–65°N (top) and 55°S–65°S (bottom) at 65 km due to Polar Mesospheric Clouds (PMC) contamination (where 350 nm residual >0.18) as a function of time. The peaks occur during austral summers in both hemispheres. Asymmetry between NH and SH results is caused by asymmetry in the PMC phase function which is stronger in the forward scattering direction. Ozone Mapping and Profiler Suite Limb Profiler views with backscattering geometry in the SH and forward scattering geometry in the NH.

show examples below. We have created an OMPS-LP temperature product sampled at one day per month during the period April 2012–June 2021 for this analysis.

6.1. Comparison With First Guess

Our algorithm starts with assimilated meteorological data (Section 3) as a first guess (FG). These data are generally considered to be of high quality below 35 km, but their quality degrades at higher altitudes due to decreases in the sensitivity and vertical resolution of operational meteorological sensors. Above ~45 km the assimilated temperature profiles are mostly based on numerical model predictions. Figures 10–13 show how our retrieved temperature profiles compared with the FG profiles.

These comparisons show generally good agreement between retrieved temperatures and assimilated temperatures below 50 km. At higher altitudes there are significant differences and systematic biases. However, the seasonal cycle amplitude and interannual variability agree with the variations in retrieved temperatures (see Figures 11 and 12). Broadly speaking, these results are consistent with other satellite sensor measurements, such as MLS. In Section 8 we show direct comparison with data from MLS and other sensors.

6.2. Comparison Between Slits

As discussed in Section 2, the OMPS-LP instrument measures using 3 slits that project to different positions on the earth. Direct comparison of the radiances between them has revealed significant differences, apparently caused by calibration errors and stray light errors. Though we have designed our algorithms to minimize the effect of these errors on retrieved temperatures, results from the different slits still differ significantly, as shown in Figure 14. These comparisons cannot discern which of the three slits performs best, but differences between them provides a measure of uncertainty in the temperature profiles retrieved from OMPS-LP data. We have analyzed the temperature retrievals from left and right slits and compared them with the data from the center slit. Results for the comparisons are shown in Figure 15. Both comparisons yield very similar results in terms of statistical parameters, about 93.2% and 99.5% of total points are found to be within the absolute difference of ±3 and ±5 K for right slit versus center slit, 96.0% and 99.6% points are found to be within the absolute difference of ±3 and

10.1029/2022EA002763

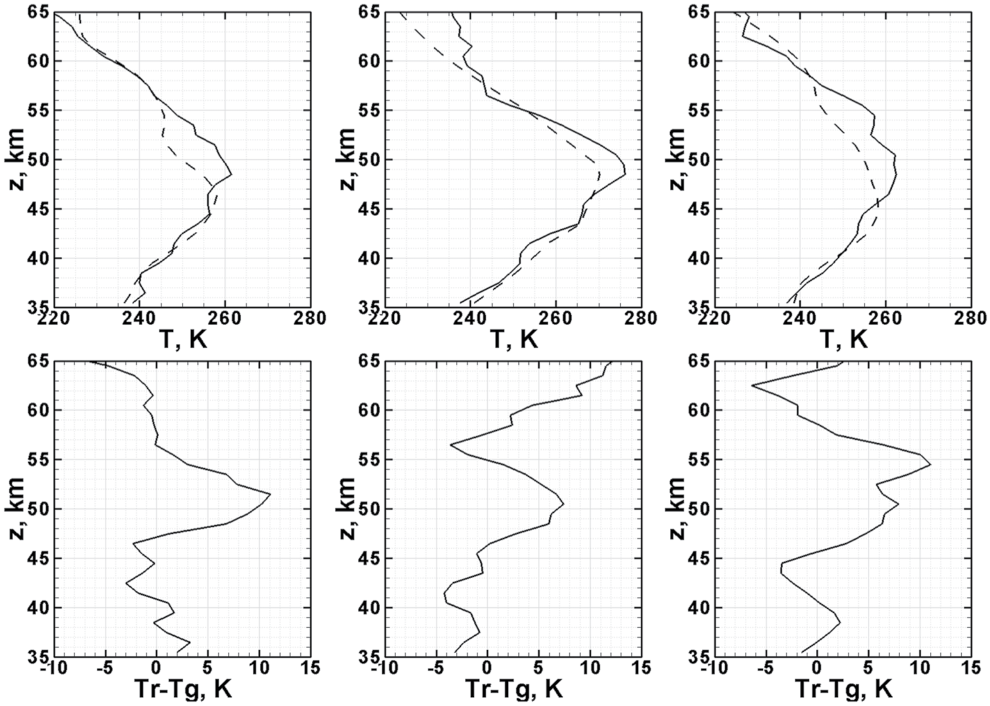

Figure 10. Comparisons of three Limb Profiler retrieved temperature profiles (T_r) with first guess profiles (T_g) at 55° S (left), 5° N (middle) and 55° N (right) for an orbit on 23 March 2017. The FG profiles are based on assimilated meteorological data. Top plots show vertical profiles of T_r (solid line) and T_g (dashed line). Bottom plots show their differences (T_r–T_g). The retrieved and FG profiles agree better at lower altitudes where the assimilated data are considered reliable. At higher altitudes there are significant differences in vertical structures. However, to determine if these structures are real one needs to compare with other datasets.

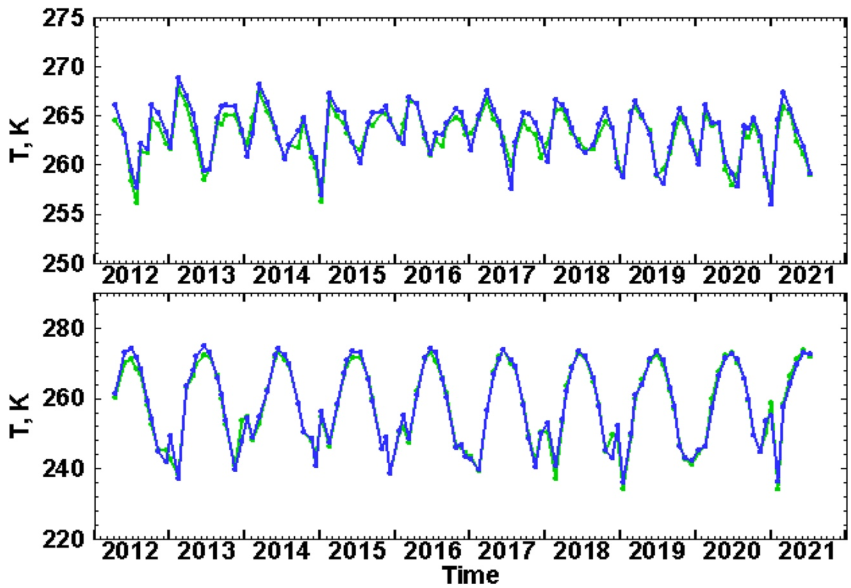

Figure 11. Time series of daily zonal mean temperatures from Limb Profiler (T_r), in blue and first guess (FG) temperatures (T_g), in green, at 45.5 km altitude in two latitude bands in 20°S–20°N (top) and 55°N–60°N (bottom) for one day per month between April 2012 and July 2021. The seasonal cycles and inter-annual variabilities agree quite well at this altitude, where assimilated data are more reliable.

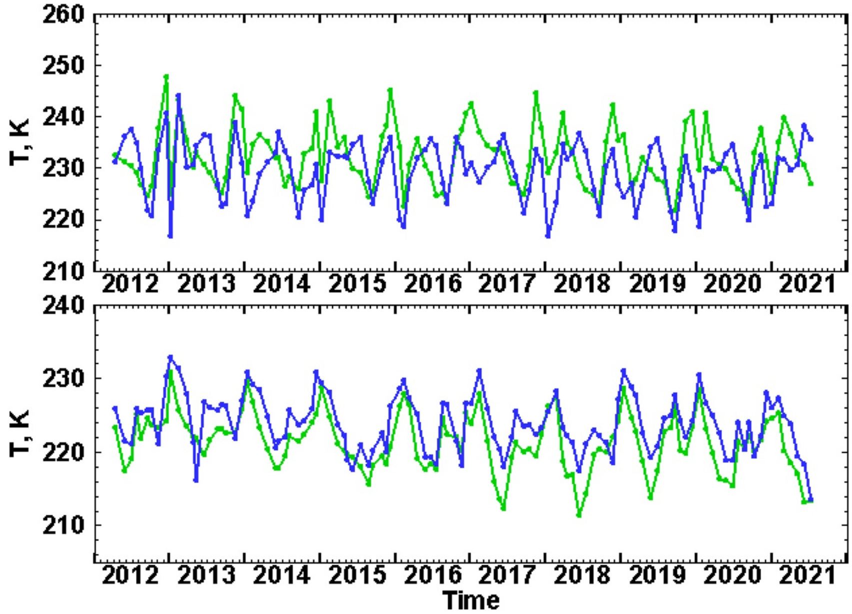

Figure 12. Same as Figure 11, but for altitude at 65.5 km. At this altitude differences with FG are larger. This is expected given the degradation in the quality of assimilated data.

±5 K for left slit versus center slit, respectively. The bias in the retrieved temperatures between the three LP slits can be calculated from differences in the linear fits shown in Figure 15.

6.3. Sensitivity to 35 km Aerosols

As noted in Section 3, 350 nm OMPS-LP radiances at 35 km are significantly affected by tropical aerosols in years when the quasibiennial oscillation (QBO) circulation lofts them to higher than typical altitudes. The density

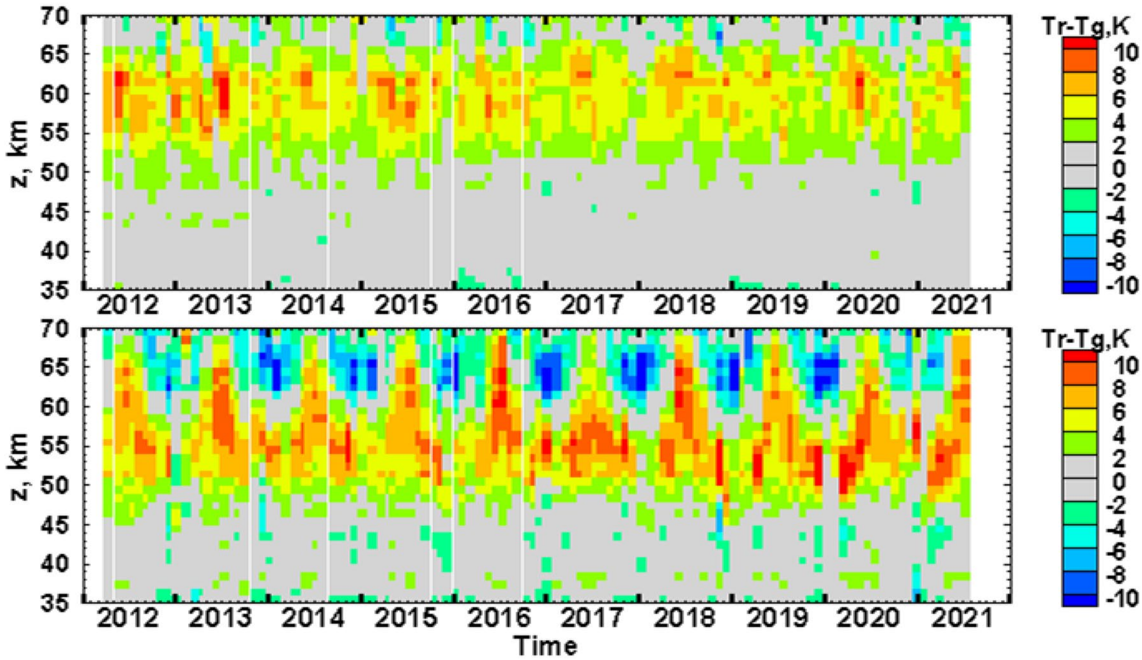

Figure 13. Time–altitude curtain plots of the differences in daily zonal mean retrieved temperatures (T_r) and first guess (T_g) for the same time period as in previous figures. The top panel is for the tropics (20°S–20°N). The bottom figure is for 55°N–60°N. The retrieved temperatures are consistently higher near 55 km in both plots, and lower at 65 km the in northern hemisphere (bottom plot), suggesting that the biases, particularly at 55 km, could be the result of uncorrected stray light errors.

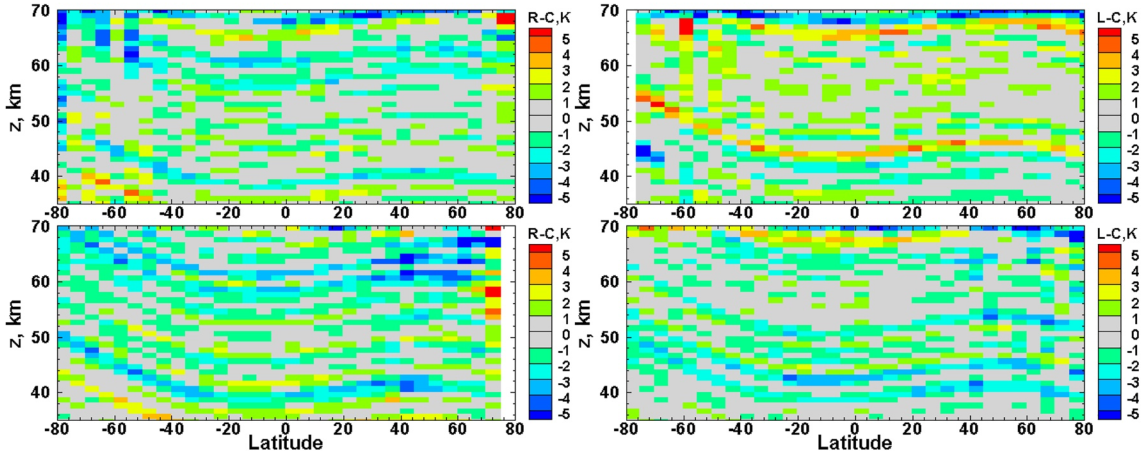

Figure 14. Latitude–altitude curtain plots of difference in the retrieved daily zonal mean temperatures from three Limb Profiler (LP) slits for 14 September 2012 (top) and 5 March 2021 (bottom). Left plots show differences between the right slit (R) and the center slit (C) and the right plot between the left slit (L) and C. The tilted stripes reflect errors in the characterization of LP sun-normalized radiances, but the source of this error is not well understood.

of these aerosols varies by an order of magnitude from year to year, but as shown in Figure 16, the difference between retrieved and first-guess temperatures is not significantly correlated with 675 nm aerosol extinction, providing confidence that algorithms to minimize the impact of aerosol on retrieved temperature are working as intended.

7. Error Analysis

We need to consider three types of errors: (a) errors in a priori profiles, (b) errors in the RTM, and (c) measurement errors. In the following section we focus primarily on estimating sensitivity of retrievals to these errors.

7.1. Effect of Errors in A Priori

The algorithm uses temperature profiles from the GMAO FP assimilation (as discussed in Section 3) both as first guess and as a priori (AP). The former is used primarily to linearize the solution. The latter is used to constrain the solution. As shown in Sections 4 and 6, the algorithm is capable of producing values that deviate considerably from AP. However, AP does get used by the algorithm at three specific places: (a) in starting of the integration of hydrostatic equation at 30.5 km (Section 3), which assumes that AP pressure at this altitude is accurate, (b)

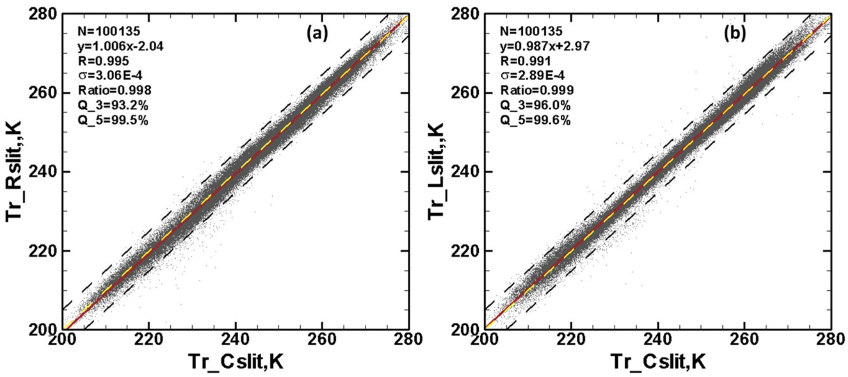

Figure 15. Comparison of the retrieved daily zonal mean temperatures between the side slits (y axis) and center slit (x axis) at 35.5–65.5 km in 65°S–65°N for one day per month between April 2012 and July 2021. (a) Right slit versus center slit. (b) Left slit versus center slit. The dark gray dots represent all data points, the yellow line represents a 1:1 relationship, and the red line shows the linear regression between the data points. The statistics are shown inside each plot, where N is the total number of data points, R is correlation coefficient, σ is the standard deviation of the differences (x–y), ratio is the ratio of y/x, Q_3 and Q_5 are the percent of total points (N) that fall within the absolute difference of ±3 and ±5 K, respectively.

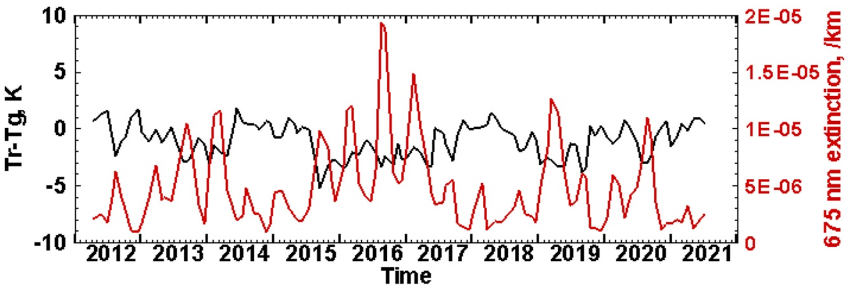

Figure 16. The red line shows daily zonal mean time series (one day per month) of 675 nm aerosol extinction at 35.5 km for the tropical latitude band (20°S–20°N) retrieved using OMPS-LP data. The black line shows time series of difference between retrieved and FG temperature (T_r–T_g) at 35.5 km. Though there is more than an order of magnitude variation in aerosol extinction, T_r–T_g difference are within ±5 K and not correlated with aerosols.

in normalization of radiances at 40.5 km, which forces the measured and calculated radiances to agree at this altitude, and (c) in extension of atmospheric profiles between 75 and 100 km for use in radiance simulations with the forward model. Figures 17–19 show that the sensitivity of the algorithm to the first two of these cases is quite small, and the effect of the third case is limited to altitudes above 70 km.

7.2. Errors in the Radiative Transfer Model (RTM)

Our RTM, as described in Section 3, assumes a Lambertian reflecting surface located at 1,013.25 hPa to account for surfaces, tropospheric clouds and aerosols. It also has no explicit correction for variation in surface pressure. The algorithm also uses a scalar code to calculate the radiance, even though it is well known that at 350 nm one needs to use a vector code that accounts for polarization to calculate the radiances accurately. Our analysis shows that altitude normalization removes the effect of errors caused by variations in surface pressure and polarization and aerosols, but the effect of three-dimensional clouds, such as narrow deep convective clouds, on altitude normalized radiance is not known, and we do not have the appropriate RT code to calculate their effects. Since these clouds are readily identified by their reflectivity ($R > 0.8$) in snow/ice-free regions, their impact on radiances might be estimated by comparison with other temperature estimates, but this effort is beyond the scope of this current work.

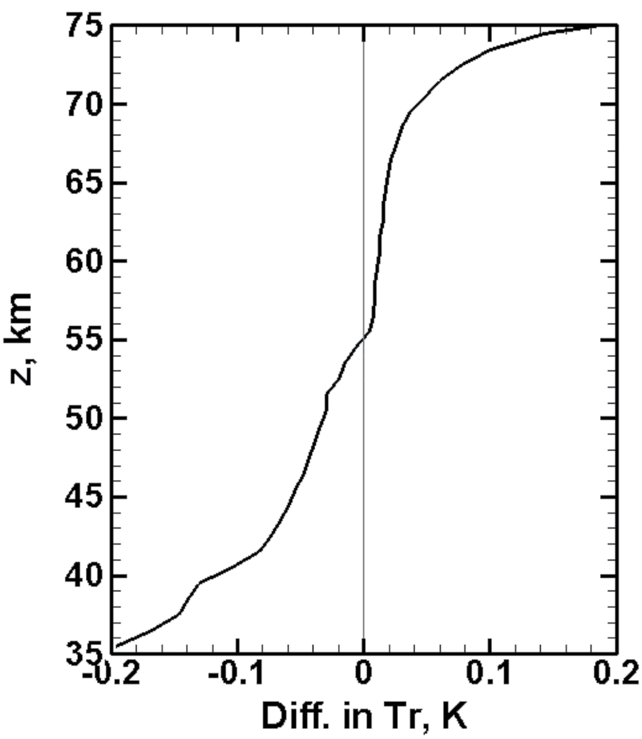

Figure 17. Change in the temperature profile due to changing the 30.5 km pressure by 1%. The algorithm starts the integration of hydrostatic equation at 30.5 km where the a priori pressures estimated using assimilated meteorological data are assumed to be accurate to within 1%.

7.3. Measurements Errors

Since we use averages of 11 LP wavelengths centered at 350 nm in our algorithm, the effect of random measurement errors is reduced. Larger errors are caused by vertical structures in radiances that vary with altitude and latitudes (as discussed in Section 5.2). The latitudinal variations appear to be caused by orbital variations of the projected limb image on the CCD. However, since the radiances have been normalized by solar irradiances measured by the same CCD their presence remains a mystery. Though their effect is also reduced by 11 wavelength averaging, the residuals errors are estimated to be ±2 K. Since the errors in individual slits are uncorrelated, they can produce ±4 K slit to slit differences, as seen in Section 6. These estimates are confirmed by results from inter-slit comparisons.

The OMPS-LP instrument also has significant stray light contamination at higher altitudes (Jaross et al., 2014). Though we have corrected for these effects some residuals effects may still be present. Figure 20 shows the sensitivity of retrieved temperatures to such an error. The error chosen for this simulation is comparable to stray light uncertainties we have observed at these altitudes.

10.1029/2022EA002763

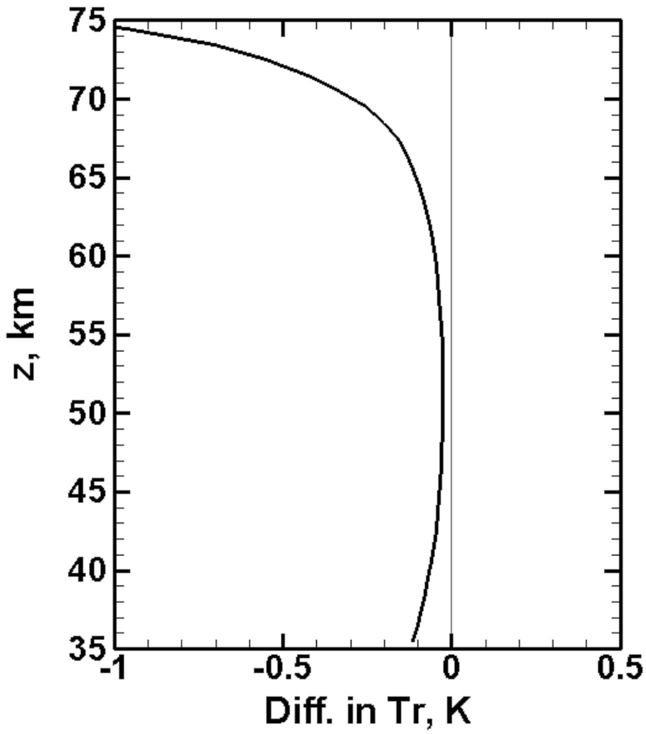

Figure 18. Effect on the retrieved temperatures of changing the normalization altitude from 40.5 to 35.5 km. The algorithm normalizes the radiance at 40.5 km to reduce errors in estimating multiple scattering.

8. Comparison With Other Sensors

Retrieved OMPS-LP temperature profiles are compared in this section with coincident profiles from four correlative data sets: Version 2 temperature profiles from Sounding of the Atmosphere Using Broadband Emission Radiometry (SABER) on the NASA TIMED satellite (Remsberg et al., 2008; Russell et al., 1999), Version 5 temperature profiles from the Microwave Limb Sounder (MLS) on the NASA Aura satellite (Livesey et al., 2020; Schwartz et al., 2008, 2020), Version 4 temperature profiles from the Atmospheric Chemistry Experiment–Fourier Transform Spectrometer (ACE) on the Canadian SCISAT satellite (Bernath et al., 2005), and lidar profiles from the Network for the Detection of Atmospheric Composition Change (NDACC) sites at Hohenpeissenberg, Germany and Mauna Loa, HI, USA (Hauchecorne and Chanin, 1980; Marlton et al., 2021; Wing et al., 2021). Both SABER and ACE-FTS measure temperature using infrared observations of carbon dioxide spectra, ACE-FTS doing so through solar occultation while SABER uses radiometry of atmospheric limb scans. MLS temperature is inferred from radiometry of millimeter-wave spectra of diatomic oxygen lines scanned through the atmospheric limb. The lidar temperature profiles are derived from atmospheric density profiles that are inferred from scattering by the atmosphere of ultraviolet laser light (Hauchecorne and Chanin, 1980).

For each OMPS-LP profile, a correlative data set profile is considered coincident if it is the closest profile in great-circle distance ($\pm\Delta d$) that is also within a set time window ($\pm\Delta t$) and latitude window ($\pm\Delta$lat) of the OMPS-LP profile. For MLS and SABER, we set $\Delta t = 3$ hr, Δlat = 4°, and $\Delta d = 1{,}320$ km. ACE-FTS has sparser sampling, so the coincidence criteria are relaxed to $\Delta t = 8$ hr, Δlat = 6° and Δd = 2200 km to produce sufficient pairs for analysis. Lidar data are geographically limited, so the coincidence criteria are further relaxed to Δt = 10 hr, Δlat = 4°, and $\Delta d = 4{,}400$ km. At most, one profile from a given correlative data set is used in these analyses for a given OMPS-LP profile. Correlative data are screened for quality based on the recommendations of the respective science teams if such screening is specified, and are interpolated to the OMPS-LP 1-km grid from 35.5 to 70.5 km. The ACE-FTS native 1-km temperature vertical grid is a superset of the OMPS-LP grid, so no interpolation is needed. The SABER native vertical temperature grid has ~0.4 km spacing and the lidar vertical grid has 0.3 km vertical spacing, so these profiles are degraded to the OMPS-LP grid resolution. The MLS temperature profiles are reported on a fixed pressure grid that has a resolution of ~1.5–5 at 35–70 km, but the actual vertical resolution of the v5 MLS temperature product at these altitudes is 5–8 km. MLS geopotential height, which is retrieved on the same pressure levels as temperature, is converted to height and used to interpolate the MLS temperature profiles to the OMPS-LP vertical height grid.

Figure 21 shows mean profiles and mean correlative profiles from coincident profile pairs of temperature profiles, based on seasonal averages over the 10-year OMPS-LP data record. We use the sample LP temperature product described in Section 6 for this analysis. Panels Figure 21a shows generally good agreement between SABER and OMPS-LP, including through the stratopause temperature maximum near 50 km. Agreement is not as good above 60 km, particularly at high latitudes. Figure 22a shows mean differences (solid) and the standard deviations of the differences (dashed) between OMPS-LP and SABER profiles; OMPS-LP is within ~1 K of SABER up to 50 km, with a global mean difference (black line) close to 0 K. There is a low bias in OMPS-LP temperature at higher levels, growing to 1–2 K above 60 km. The larger scatter in mean difference above 60 km appears to reflect both a noisier retrieval at these levels and occasional large (non-Gaussian) outliers. The low bias in OMPS-LP relative to SABER of 3–5 K above ~56 km at high southern latitudes (90–60S) bin in austral spring (Figure 22a SON) is not due to the influence of a few outliers and is not understood. The standard deviation in the OMPS minus SABER differences (Figure 22a dashed lines) are generally 3–5 K below 60 km, but are 5–7 K in the winter high latitudes. High altitude high outliers in the standard deviations (e.g., Figure 22a SON at 62 km) are generally due to individual high outlier OMPS-LP retrieved temperatures. It is believed that a more-complete implementation of the screening described in Section 5.1 will reduce the number of outliers in the OMPS-LP data set. In comparisons

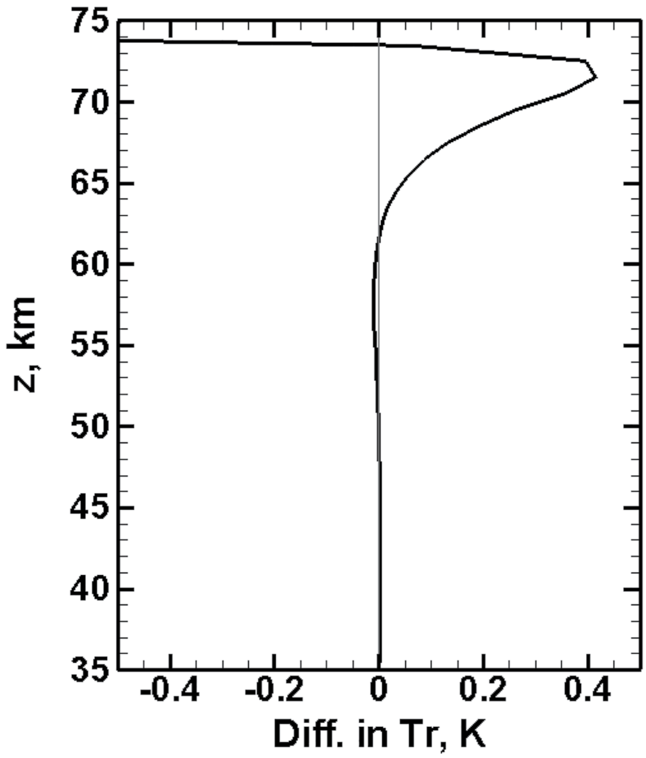

Figure 19. Effect of changing the calculated radiances at 75.5 km by 5%. These radiances are calculated using AP T profiles above 75 km. The changes are small compared to measurement errors are localized above 70 km.

shown in this section we exclude profiles that have retrieved temperature at any level exceeding 350 K, however, in the OMPS-LP–SABER comparisons, this additional screening removes only three profiles and has minimal impact on the statistics of comparisons. Figure 23a show scatter plots of SABER versus OMPS-LP temperatures for selected levels, with a logarithmic color scale to demonstrate the structure of the joint probability distribution while also showing individual outliers. The increasing noisiness of the OMPS-LP retrieval above 60 km is evident, both in the broadening of the distributions along the 1:1 line and in the greater number in outliers.

Figures 21 and 22b show MLS and OMPS-LP coincident temperature profiles and mean and standard deviations of their differences, respectively. Agreement is not as good as it is for SABER, with a vertically oscillating bias structure of ∼5 K peak-to-peak with a ∼15 km vertical wavelength that is particularly evident in the difference plots of Figure 22b. A high bias is also present that grows with altitude in OMPS-LP with respect to MLS. MLS temperature has lower vertical resolution at 35–70 km than do the other correlative data sets, and MLS does not resolve the stratopause as well as they do. Given the lack of the vertical oscillations in differences in other correlative data, the vertically oscillating biases seen in OMPS-MLS differences almost certainly result from a deficiency of the MLS data (Wing et al., 2018), not of the OMPS-LP data. Despite these biases, the scatter about the mean OMPS-MLS difference (the dashed lines of Figure 22b) is slightly smaller than that of the OMPS-SABER differences. The larger OMPS-SABER scatter likely results from greater variability in the higher resolution SABER temperature profiles compared to the smoother MLS profiles. Scatter plots of MLS versus OMPS-LP in Figure 23b are similar to those of Figure 23a for SABER, albeit with shifts from the 1:1 lines reflecting MLS biases at different levels. The expanded distribution due to OMPS-LP outliers, particularly above 60 km, are quite similar in Figures 23a and 23b. Note that the sets of OMPS-LP profiles coincident with the two correlative data sets are completely distinct, but their outlier statistics are consistent.

The ACE-FTS solar occultation technique produces 1–2 orders of magnitude fewer coincident profile pairs than are found for SABER and MLS, but the agreement seen in Figure 22c global mean (the black line) is still typically within ∼1.5 K below 55 km. Scatter among the latitudinally/seasonally binned mean profiles may result, at least in part, from there being fewer available profiles pairs and from the need to relax coincidence criteria to get even this many pairs. A low bias above 55 km of ∼2 K in OMPS-LP temperature relative to ACE-FTS temperature is similar to that observed in the SABER comparisons (Figure 22a). Scatter plots of ACE-FTS temperature versus OMPS-LP temperature (Figure 23c) show larger scatter about the 1:1 lines than is seen in analogous SABER and MLS panels, and the rare outliers in OMPS-LP are not evident due to the limited number of samples.

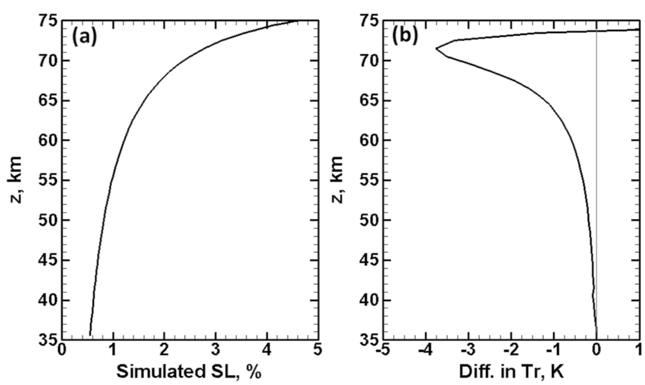

Figure 20. Sensitivity to stray light (SL) errors. Left panel shows a simulated SL error in radiances in percent estimated by assuming that the absolute signal error is constant across all altitudes. The right panel shows its impact on the retrieved temperatures. The errors are largely confined to altitudes above 70 km.

Lidar coincident profile pairs (Figures 21 and 22d) are even fewer in number than those of ACE-FTS, with between 10 and 22 profile pairs in a given seasonal/latitudinal bin. The Mauna Loa (19.54°N) coincidences and the Hohenpeissenberg profiles (47.8°N) comprise the data in the tropical and northern midlatitude bins, respectively. As noted above, while the criteria for identifying coincidences are loosened for lidar measurements (Δt = 10 hr, Δd = 4,400 km), the number of coincident pairs is still so limited that breaking out Figure 22d by seasonal subpanels results in noisy plots that are difficult to interpret. However, the all-season averages shown in Figure 22d are well behaved, and generally are remarkably consistent with mean biases seen in Figure 22a for SABER differences and (to a slightly lesser extent) in Figure 22c for ACE-FTS differences. Lidar data are vertically degraded to the OMPS-LP 1-km grid using a linear least square fit to smooth sub-kilometer

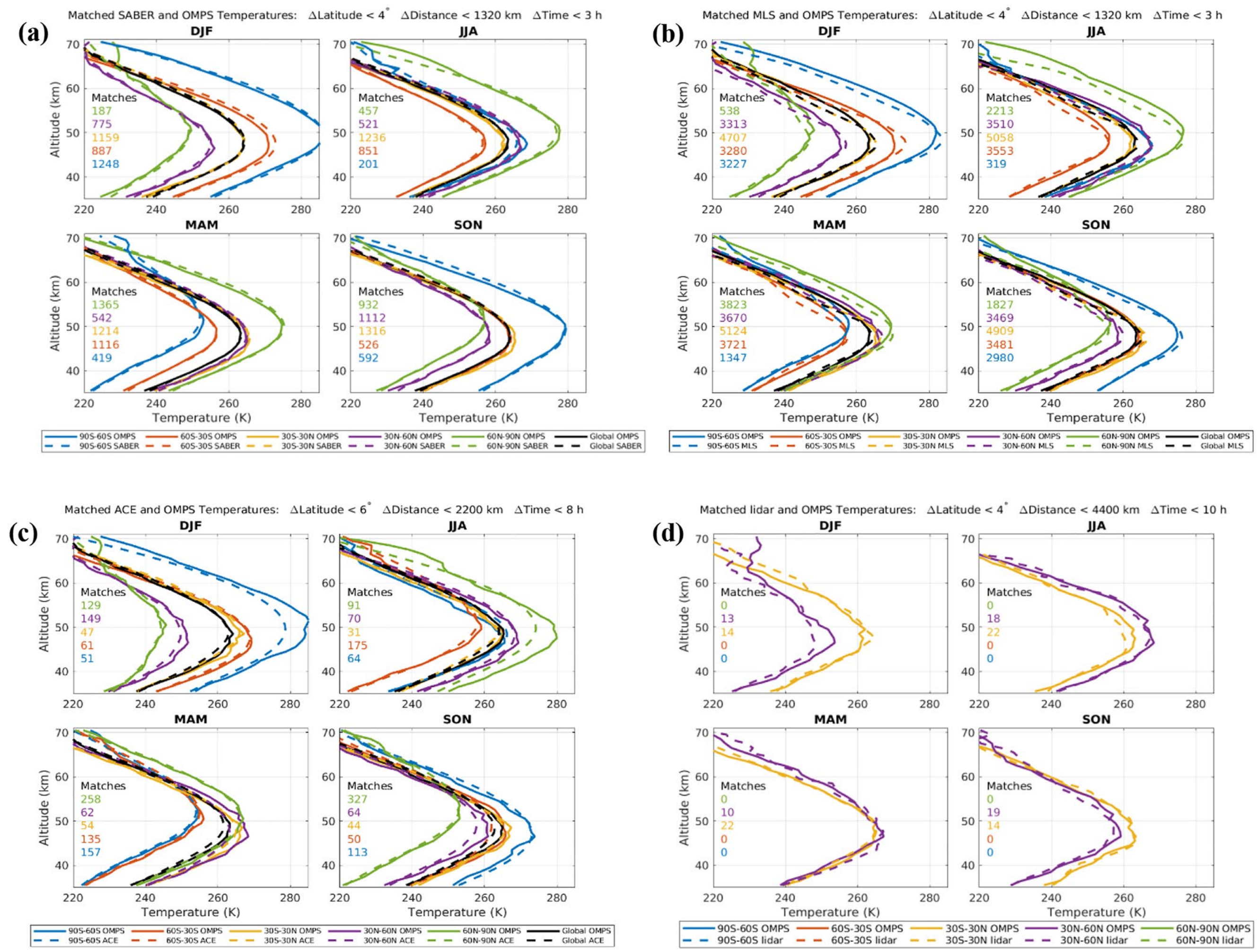

Figure 21. Ozone Mapping and Profiler Suite Limb Profiler (OMPS-LP) temperature profiles are compared to coincident profiles from (a) Sounding of the Atmosphere Using Broadband Emission Radiometry, (b) Microwave Limb Sounder, (c) Atmospheric Chemistry Experiment–Fourier Transform Spectrometer, and (d) lidar. In all cases, the solid lines are OMPS-LP and the dashed lines are the correlative data, the different colors are latitude bins and the four subpanels are seasons.

vertical variability, but the lidar–OMPS-LP differences still have more variability (dashed lines of Figure 22d) than do the other correlative data. There may be atmospheric variability at the 1-km vertical scale that is captured by the lidar, but not by the other instruments. The use of a $\Delta t = 10$ hr for the coincidence criterion could also contribute to noisy coincidence differences, since variability due to tides and gravity waves can be considerable in the mesosphere at that timescale. Leblanc et al. (1999) report $a \pm 3$ K tidal amplitude below 70 km at Mauna Loa. All-season scatter plots in Figure 23d show that the tropical Mauna Loa profiles at a given level have significantly less variability than do the mid-latitude Hohenpeissenberg profiles, with less scatter about the 1:1 line, which likely reflects both the greater atmospheric variability at mid-latitudes and the lower power laser used at Hohenpeissenberg, which gives poorer photon-counting statistics. Despite this variability, the mean OMPS-LP minus lidar bias shown in Figure 22d is consistent with those seen in Figure 22a for SABER and Figure 22c for ACE-FTS.

Figures 24a–24c show latitudinally and seasonally binned histograms of temperature from OMPS-LP, MLS and SABER, respectively. In each of these panels, the darkest blue color represents a single observation in a 5-K bin while the darkest red color typically represents several orders of magnitude more observations per bin. The variability seen in the histograms from the three instruments is generally consistent. OMPS-LP has more outliers (isolated dark blue points) than do the other instruments, particularly in the 60–30S bins, which again suggests that the screening of Section 5.1 has not completely removed impacts of the South Atlantic Anomaly. As noted above, a more complete implementation of the screening algorithm may improve this behavior. The Arctic

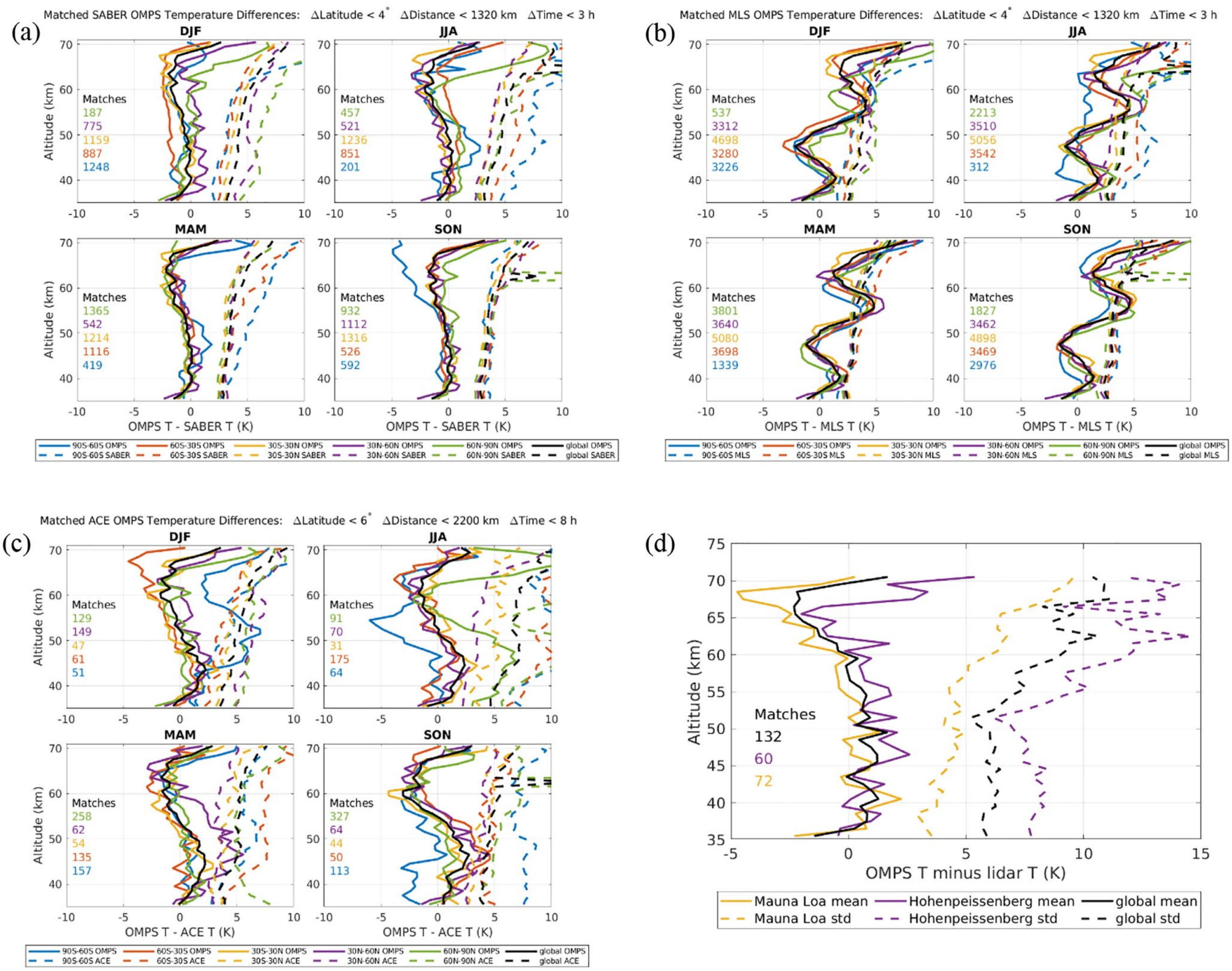

Figure 22. Ozone Mapping and Profiler Suite Limb Profiler temperature profiles minus coincident profiles from (a) Sounding of the Atmosphere Using Broadband Emission Radiometry, (b) Microwave Limb Sounder, (c) Atmospheric Chemistry Experiment–Fourier Transform Spectrometer, and (d) lidar. In all cases, the solid lines are mean differences and the dashed lines are the standard deviation of the differences, and as in Figure 21, the different colors are latitude bins and the four subpanels are seasons. Lidar profiles are shown on a single panel for all seasons due to the limited number of coincidences.

summer (Figures 24a 60–90N JJA) and Antarctic summer (Figures 24a 90–60S DJF) both have distributions of high outliers at the highest altitudes, at times exceeding 300 K, which are not seen in corresponding MLS or SABER histograms. As can be seen in Figure 24d, these high anomalies repeat every summer, reminiscent of the seasonal pattern in Figure 9 showing where PMC-impacted profiles were identified and discarded. These high outliers are almost certainly due to impacts of PMCs that have not been completely screened out by the algorithms of Section 5.3.

In summary, apart from some vertical bias structure in the MLS temperature correlative profiles, the four correlative data sets give a consistent picture of OMPS-LP retrieved temperature. OMPS-LP mean temperatures generally have biases of ~1 K or less from 31.5 to 50 km relative to SABER, ACE-FTS and lidar. A low bias in OMPS-LP temperature begins to be apparent above 50 km, reaching ~2-K magnitude above 60 km. A low bias of ~1K in OMPS-LP at 35.5 km and a high bias of ~2 K AT 70.5 km, the lowest and highest levels of the retrieval, are also apparent. Scatter between OMPS-LP and SABER and MLS correlative profiles is typically 3–4 K below ~55 km, though it can be larger seasonally and latitudinally. ACE-FTS and lidar coincident profile differences are noisier, typically 5–6 K. For all correlative data sets, scatter in the differences increases somewhat above 55 km, but outlier retrieval values also become more common at higher retrieval levels (Figure 24). Outliers in the OMPS-LP zonal/seasonal temperature histograms indicate that some profiles impacted by the SAA and by PMCs have evaded screening.

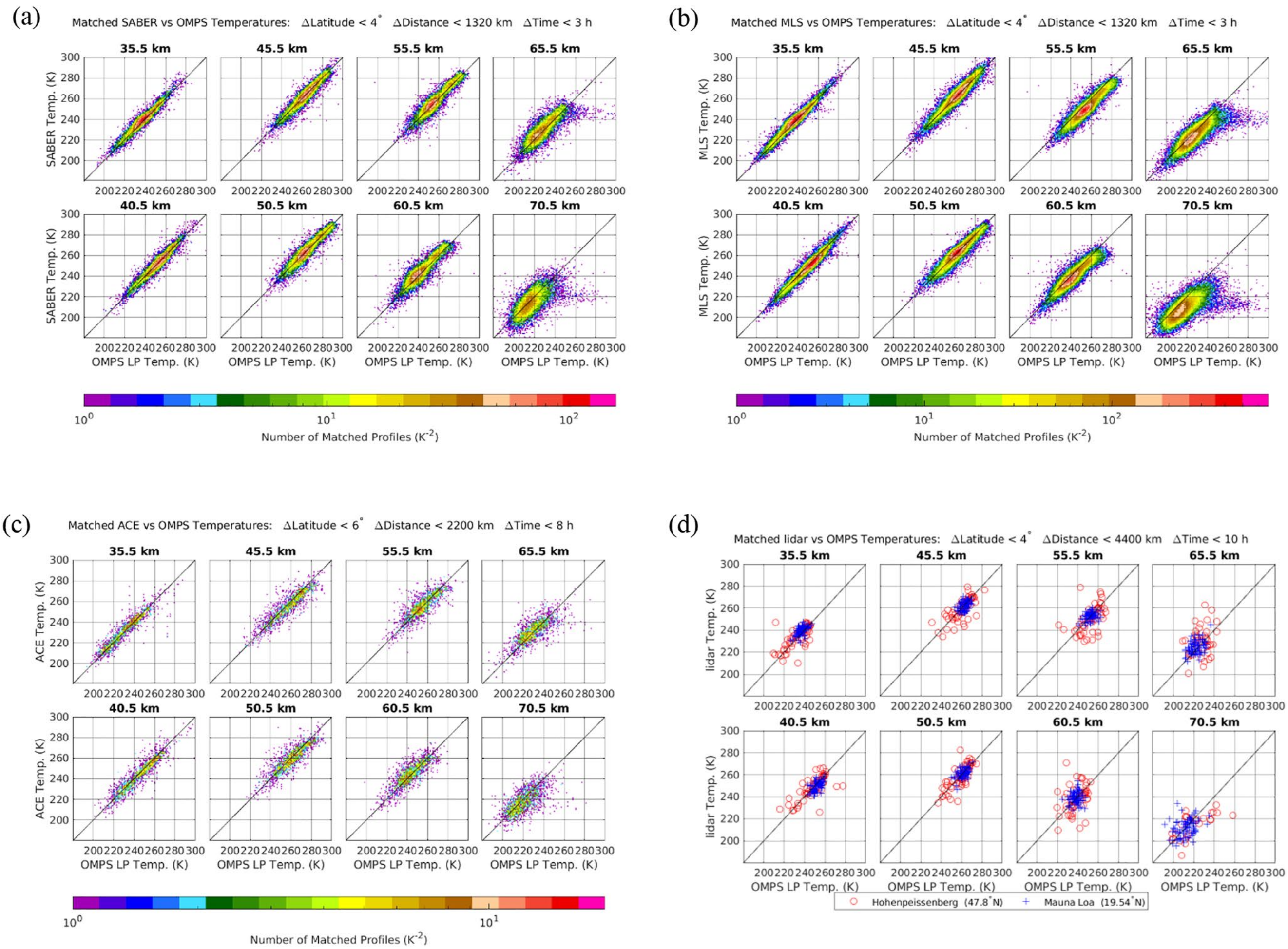

Figure 23. Ozone Mapping and Profiler Suite temperature profiles scattered against coincident profiles from (a) Sounding of the Atmosphere Using Broadband Emission Radiometry (SABER), (b) Microwave Limb Sounder (MLS), (c) Atmospheric Chemistry Experiment–Fourier Transform Spectrometer (ACE-FTS) and (d) lidar. For comparisons with MLS, SABER and ACE-FTS, color denotes the number of points per bin. For the lidar panels, (d), color is used to distinguish data from the two stations.

9. Summary, Conclusion, and Future Work

We have described an algorithm to retrieve vertical temperature profiles from OMPS-LP radiances in the 35–70 km altitude range. We have currently processed one day of data per month for evaluation purposes. We plan to process the entire 10 year record of LP data collected since 2012, using a recently updated Level 1 calibration and improved screening tests to identify and eliminate anomalous profiles. We use a heuristic method for correcting the measured radiances for multiple scattering effects, and we use Chahine inversion method to retrieve atmospheric density profiles from measured radiances. The best way to determine the validity of our methodology is to compare with other algorithms that do not rely on these approaches and this project will be undertaken in the future.

We have compared our results with four other instruments (SABER, MLS, ACE, lidar) that measure temperature in the upper stratosphere and lower mesosphere. All of the measurements are consistent within reasonable bounds of the expected uncertainty.

Sun-normalized LP radiances show distinct vertical structures that vary with latitude and time. Though we have designed our algorithm to minimize their impact, they remain the largest source of systematic error in retrieving temperature profiles from OMPS-LP. However, these errors mostly produce bias in the retrieved temperatures; the errors in estimating time dependence are relatively small. We anticipate learning more about the source of these errors by comparing with the second OMPS-LP instrument that was launched in November 2022.

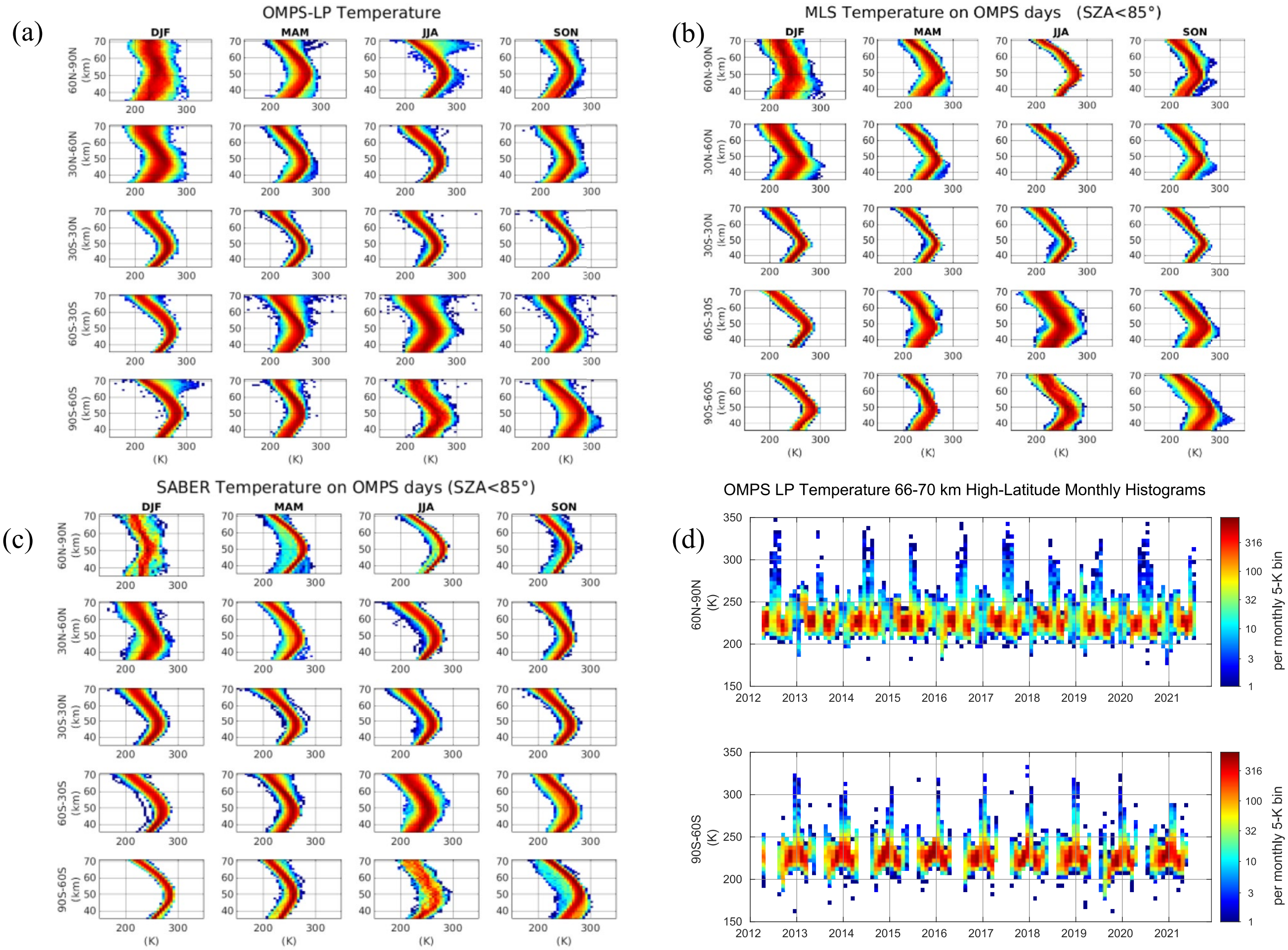

Figure 24. Histograms by latitude band and season for (a) Ozone Mapping and Profiler Suite temperature, (b) Microwave Limb Sounder (MLS) temperature, and (c) Sounding of the Atmosphere Using Broadband Emission Radiometry (SABER) temperature. MLS and SABER observations are restricted to daytime (solar zenith angle less than 85°). Color scales are logarithmic, with the darkest blue representing single observations and the darkest red representing 2,000–3,000 observations per 5 K bin. Panels (d) are monthly histograms of high-altitude (66–70 km), high-latitude observations, with summer high outliers indicating persisting impacts of polar mesospheric clouds.

Data Availability Statement

ACE-FTS observations are available (Sheese & Walker, 2020, https://doi.org/10.5683/SP2/BC4ATC), following registration, from http://www.ace.uwaterloo.ca. Lidar data are available at https://www-air.larc.nasa.gov/missions/ndacc/data.html or through a search tools available on the NDACC website (www.ndacc.org). MLS data are available at the NASA GSFC DISC (https://disc.gsfc.nasa.gov). SABER data are available at http://saber.gats-inc.com/.

Acknowledgments
We thank the OMPS-LP team at NASA Goddard and Science and Systems and Applications, Inc. (SSAI) for help in producing the data used in this research. We thank the SABER science team for making the SABER temperature record available. The Atmospheric Chemistry Experiment (ACE), also known as SCISAT, is a Canadian-led mission mainly supported by the Canadian Space Agency. Lidar data used in this publication were obtained

References

Bailey, S. M., Thurairajah, B., Hervig, M. E., Siskind, D. E., Russell, J. M., III., & Gordley, L. L. (2021). Trends in the polar summer mesosphere temperature and pressure altitude from satellite observations. *Journal of Atmospheric and Solar-Terrestrial Physics*, *220*, 105650. https://doi.org/10.1016/j.jastp.2021.105650

Bernath, P. F., McElroy, C. T., Abrams, M. C., Boone, C. D., Butler, M., Camy-Peyret, C., et al. (2005). J.: Atmospheric Chemistry experiment (ACE): Mission overview. *Geophysical Research Letters*, *32*(15), L15S01. https://doi.org/10.1029/2005gl022386

Chahine, M. (1970). Inverse problems in radiative transfer: A determination of atmospheric parameters. *Journal of the Atmospheric Sciences*, *27*(6), 960–967. https://doi.org/10.1175/1520-0469(1970)027<0960:ipirtd>2.0.co;2

Chen, Z. (2022). First observations of mesospheric OH emission profiles from OMPS/LP. *Journal of the Atmospheric Sciences*, *79*(4), 1057–1067. https://doi.org/10.1175/jas-d-21-0239.1

Chen, Z., Bhartia, P. K., Loughman, R., Colarco, P., & DeLand, M. (2018). Improvement of stratospheric aerosol extinction retrieval from OMPS/LP using a new aerosol model. *Atmospheric Measurement Techniques*, *11*(12), 6495–6509. https://doi.org/10.5194/amt-11-6495-2018

from Thierry Leblanc and Wolfgang Steinbrecht as part of the Network for the NDACC. We thank Steinbrecht for useful comments. Research carried out at the Jet Propulsion Laboratory, California Institute of Technology, was performed under a contract with the National Aeronautics and Space Administration. This research was supported by the NASA proposal "Improving the OMPS-LP Cloud Heights and Developing Additional LP Products" (Grant 80NSSC21K1965, PI: Mark Schoeberl). Zhong Chen and Matthew DeLand were also supported by the NASA contract NNG17HP01C.

Chen, Z., Bhartia, P. K., Torres, O., Jaross, G., Loughman, R., DeLand, M., et al. (2020). Evaluation of the OMPS/LP stratospheric aerosol extinction product using SAGE III/ISS observations, Atmos. *Measurement Techniques*, *13*(6), 3471–3485. https://doi.org/10.5194/amt-13-3471-2020

Chen, Z., DeLand, M., & Bhartia, P. K. (2016). A new algorithm for detecting cloud height using OMPS/LP measurements. *Atmospheric Measurement Techniques*, *9*(3), 1239–1246. https://doi.org/10.5194/amt-9-1239-2016

Clancy, R. T., Rusch, D. W., & Callan, M. T. (1994). Temperature minima in the average thermal structure of the middle mesosphere (70–80 km) from analysis of 40- to 92-km SME global temperature profiles. *Journal of Geophysical Research*, *99*(D9), 19001–19020. https://doi.org/10.1029/94JD01681

DeLand, M. T., & Gorkavyi, N. (2020). PMC observations from the OMPS limb profiler. *Journal of Atmospheric and Solar-Terrestrial Physics*, *213*, 105505. https://doi.org/10.1016/j.jastp.2020.105505

Flynn, L. E., Seftor, C. J., Larsen, J. C., & Xu, P. (2007). The ozone mapping and profiler suite. In J. J. Qu, W. Gao, M. Kafatos, R. E. Murphy, & V. V. Salomonson (Eds.), *Earth science satellite remote sensing* (pp. 279–296). Springer. https://doi.org/10.1007/978-3-540-37293-6

Gelaro, R., McCarty, W., Suárez, M. J., Todling, R., Molod, A., Takacs, L., et al. (2017). The modern-era retrospective analysis for research and Applications, version 2 (MERRA-2). *Journal of Climate*, *30*(14), 5419–5454. https://doi.org/10.1175/JCLI-D-16-0758.1

Hauchecorne, A., Blanot, L., Wing, R., Keckhut, P., Khaykin, S., Bertaux, J.-L., et al. (2019). A new MesosphEO data set of temperature profiles from 35 to 85km using Rayleigh scattering at limb from GOMOS/ENVISAT daytime observations. *Atmospheric Measurement Techniques*, *12*(1), 749–761. https://doi.org/10.5194/amt-12-749-2019

Hauchecorne, A., & Chanin, M. L. (1980). Density and temperature profiles obtained by lidar between 35-km and 70-km. *Geophysical Research Letters*, *7*(8), 565–568. https://doi.org/10.1029/gl007i008p00565

Jaross, G., Bhartia, P. K., Chen, G., Kowitt, M., Haken, M., Chen, Z., et al. (2014). OMPS Limb Profiler instrument performance assessment. *Journal of Geophysical Research: Atmospheres*, *119*(7), 4399–4412. https://doi.org/10.1002/2013JD020482

Kramarova, N. A., Bhartia, P. K., Jaross, G., Moy, L., Xu, P., Chen, Z., et al. (2018). Validation of ozone profile retrievals derived from the OMPS LP version 2.5 algorithm against correlative satellite measurements. *Atmospheric Measurement Techniques*, *11*(5), 2837–2861. https://doi.org/10.5194/amt-11-2837-2018

Leblanc, T., McDermid, I. S., & Ortland, D. A. (1999). Lidar observations of the middle atmospheric thermal tides and comparison with HRDI and GSWM. Part II: October observations at Mauna Loa (19.5°N). *Journal of Geophysical Research*, *104*(D10), 11931–11938. https://doi.org/10.1029/1999jd900008

Li, T., Yue, J., Russell, J. M., III, & Zhang, X. (2020). Long-term trend and solar cycle in the middle atmosphere temperature revealed from merged HALOE and SABER datasets. *Journal of Atmospheric and Solar-Terrestrial Physics*, *212*, 105506. https://doi.org/10.1016/j.jastp.2020.105506

Livesey, N. J., Read, W. G., Wagner, P. A., Froidevaux, L., Santee, M. L., Schwartz, M. J., et al. (2020). *Version 5.0x level 2 and 3 data quality and description document (Tech. Rep. No. JPL D-105336 Rev. A)*. Jet Propulsion Laboratory. Retrieved from http://mls.jpl.nasa.gov

Loughman, R., Bhartia, P. K., Chen, Z., Xu, P., Nyaku, E., & Taha, G. (2018). The ozone mapping and profiler suite (OMPS) limb profiler (LP) version 1 aerosol extinction retrieval algorithm: Theoretical basis. *Atmospheric Measurement Techniques*, *11*(5), 2633–2651. https://doi.org/10.5194/amt-11-2633-2018

Loughman, R., Flittner, D., Nyaku, E., & Bhartia, P. K. (2015). Gauss-Seidel limb scattering (GSLS) radiative transfer model development in support of the Ozone Mapping and Profiler Suite (OMPS) limb profiler mission. *Atmospheric Chemistry and Physics*, *15*(6), 3007–3020. https://doi.org/10.5194/acp-15-3007-2015

Marlton, G., Charlton-Perez, A., Harrison, G., Polichtchouk, I., Hauchecorne, A., Keckhut, P., et al. (2021). Using a network of temperature lidars to identify temperature biases in the upper stratosphere in ECMWF reanalyses. *Atmospheric Chemistry and Physics*, *21*(8), 6079–6092. https://doi.org/10.5194/acp-21-6079-2021

Mateer, C., Heath, D., & Krueger, A. (1971). Estimation of total ozone from satellite measurements of backscattered ultraviolet Earth radiance. *Journal of the Atmospheric Sciences*, *28*(7), 1307–1311. https://doi.org/10.1175/1520-0469(1971)028<1307:eotofs>2.0.co;2

McPeters, R. D., Janz, S. J., Hilsenrath, E., Brown, T. L., Flittner, D. E., & Heath, D. F. (2000). The retrieval of O_3 profiles from limb scatter measurements: Results from the shuttle ozone limb sounding experiment. *Geophysical Research Letters*, *27*(17), 2597–2600. https://doi.org/10.1029/1999gl011342

Rault, D. F., & Loughman, R. P. (2013). The OMPS limb profiler environmental data record algorithm theoretical basis document and expected performance. *IEEE Transactions on Geoscience and Remote Sensing*, *51*(5), 2505–2527. https://doi.org/10.1109/tgrs.2012.2213093

Remsberg, E. E., Marshall, B. T., Garcia-Comas, M., Krueger, D., Lingenfelser, G. S., Martin-Torres, J., et al. (2008). Assessment of the quality of the Version 1.07 temperature-versus-pressure profiles of the middle atmosphere from TIMED/SABER. *Journal of Geophysical Research*, *113*, D17. https://doi.org/10.1029/2008jd010013

Roble, R. G., & Dickinson, R. E. (1989). How will changes in carbon dioxide and methane modify the mean structure of the mesosphere and thermosphere? *Geophysical Research Letters*, *16*(12), 1441–1444. https://doi.org/10.1029/gl016i012p01441

Russell, J. M., Mlynczak, M. G., Gordley, L. L., Tansock, J., & Esplin, R. (1999). An overview of the SABER experiment and preliminary calibration results. *Proceedings of SPIE - The International Society for Optical Engineering*, *3756*, 277–288.

Schwartz, M., Livesey, N., & Read, W. (2020). *MLS/Aura level 2 temperature V005*. Goddard Earth Sciences Data and Information Services Center (GES DISC). https://doi.org/10.5067/Aura/MLS/DATA2520

Schwartz, M. J., Lambert, A., Manney, G. L., Read, W. G., Livesey, N. J., Froidevaux, L., et al. (2008). Validation of the Aura microwave limb sounder temperature and geopotential height measurements. *Journal of Geophysical Research*, *113*(D15), D15S11. https://doi.org/10.1029/2007JD008783

Sheese, P. E., Strong, K., Llewellyn, E. J., Gattinger, R. L., Russell, J. M., III, Boone, C., et al. (2012). Assessment of the quality of OSIRIS mesospheric temperatures using satellite and ground-based measurements. *Atmospheric Measurement Techniques*, *5*(12), 2993–3006. https://doi.org/10.5194/amt-5-2993-2012

Sheese, P., & Walker, K. (2020). Data quality flags for ACE-FTS Level 2 Version 4.1/4.2 data set. [Dataset]. Borealis. https://doi.org/10.5683/SP2/BC4ATC

Shepherd, M. G., Reid, B., Zhang, S., Solheim, B. H., Shepherd, G. G., Wickwar, V. B., & Herron, J. P. (2001). Retrieval and validation of mesospheric temperatures from Wind Imaging Interferometer observations. *J. Geophys. Res.Space*, *106*(A11), 24813–24829. https://doi.org/10.1029/2000JA000323

Taha, G., Loughman, R., Zhu, T., Thomason, L., Kar, J., Rieger, L., & Bourassa, A. (2021). TOMPS LP Version 2.0 multi-wavelength aerosol extinction coefficient retrieval algorithm. *Atmospheric Measurement Techniques*, *14*(2), 1015–1036. https://doi.org/10.5194/amt-14-1015-2021,2021

Whiteway, J. A., & Carswell, A. I. (1995). Lidar observations of gravity wave activity in the upper stratosphere over Toronto. *Journal of Geophysical Research*, *100*(D7), 14113–14124. https://doi.org/10.1029/95jd00511

Wing, R., Godin-Beekmann, S., Steinbrecht, W., McGee, T. J., Sullivan, J. T., Khaykin, S., et al. (2021). Evaluation of the new DWD ozone and temperature lidar during the Hohenpeißenberg Ozone Profiling Study (HOPS) and comparison of results with previous NDACC campaigns. *Atmospheric Measurement Techniques*, *14*(5), 3773–3794. https://doi.org/10.5194/amt-14-3773-2021

Wing, R., Hauchecorne1, A., Keckhut, P., Godin-Beekmann, S., Khaykin, S., & McCullough, E. (2018). Lidar temperature series in the middle atmosphere as a reference data set – Part 2: Assessment of temperature observations from MLS/Aura and SABER/TIMED satellites. *Atmospheric Measurement Techniques*, *11*(12), 6703–6717. https://doi.org/10.5194/amt-11-6703-2018

ZhaoSheng, X. R. Z., Shi, H. Q., Weng, L. B., & Liao, Q. X. (2020). Long term trends and solar responses of the mesopause temperatures observed by SABER during the 2002–2019 period. *Journal of Geophysical Research: Atmospheres*, *125*(11). https://doi.org/10.1029/2020JD032418